

LOW MASS STARS AND BROWN DWARFS IN NGC 2024: CONSTRAINTS ON THE SUBSTELLAR MASS FUNCTION

JOANNA L. LEVINE¹, AARON STEINHAEUER², RICHARD J. ELSTON³, AND ELIZABETH A. LADA,
Department of Astronomy, University of Florida, Gainesville, FL 32611-2055
Accepted for publication in the Astrophysical Journal

ABSTRACT

We present results from a near-infrared spectroscopic study of candidate brown dwarfs and low mass stars in the young cluster NGC 2024. Using FLAMINGOS on the KPNO 2.1m and 4m telescopes, we have obtained spectra of ~ 70 new members of the cluster and classified them via the prominent J and H band water absorption features. Derived spectral types range from $\sim M1$ to later than $M8$ with typical classification errors of 0.5-1 subclasses. By combining these spectral types with JHK photometry, we place these objects on the H-R diagram and use pre-main sequence evolutionary models to infer masses and ages. The mean age for this low mass population of NGC 2024 is 0.5 Myr and derived masses range from ~ 0.7 - $0.02 M_{\odot}$ with 23 objects falling below the hydrogen-burning limit. The logarithmic mass function rises to a peak at $\sim 0.2 M_{\odot}$ before turning over and declining into the substellar regime. There is a possible secondary peak at $\sim 0.035 M_{\odot}$ however the errors are also consistent with a flat IMF in this region. The ratio of brown dwarfs to stars is similar to that found in the Trapezium but roughly twice the ratio found in IC 348, leading us to conclude that the substellar IMF in young clusters may be dependent on the local star forming environment.

Subject headings: infrared: stars — open clusters and associations: individual (NGC 2024) — stars: low-mass, brown dwarfs — stars: luminosity function, mass function — stars: pre-main sequence

1. INTRODUCTION

Brown dwarfs were first postulated four decades ago by Kumar (1963) but their existence was not confirmed until ~ 30 years later (Oppenheimer et al. 1995; Nakajima et al. 1995; Rebolo et al. 1995). Now brown dwarfs are observed in abundance both in the Galactic field (e.g. Kirkpatrick et al. 1999; Delfosse et al. 1999; Reid et al. 1999; Chabrier 2002) and in young star forming regions (e.g. Wilking et al. 1999; Lucas & Roche 2000; Muench et al. 2001; Barrado y Navascués et al. 2004). However, the origin of these objects is still unclear. Do brown dwarfs form in a manner similar to their stellar counterparts or more akin to their planetary cousins? What mechanism drives brown dwarf formation and does it depend on the star forming environment? Recently many theories of brown dwarf formation have been proposed, including turbulent fragmentation of a molecular cloud (Padoan & Nordlund 2002), ejection of protostellar embryos (Reipurth & Clarke 2001), gravitational disk instabilities (Pickett et al. 2000), and photo-erosion of prestellar cores (Whitworth & Zinnecker 2004). In depth studies of brown dwarf properties, including their spatial distribution, disk frequency, and characteristics of the substellar initial mass function (IMF) are needed to distinguish between these formation scenarios.

The youngest star clusters (e.g. $\tau < 5$ Myr) are ideal laboratories for the study of brown dwarfs. Theoretical models predict that the luminosities of contracting, pre-main sequence (PMS) brown dwarfs will be 2-3 magnitudes brighter than field brown dwarfs of the same mass (Burrows et al. 1997, 2001), making even the lowest mass objects detectable at distances out to the nearest star forming regions (150-500 pc). The high spatial density in most clusters ensures efficient acquisition of a statistically significant sample of sources. Fi-

nally, the youngest clusters have yet to undergo significant dynamical evolution thus allowing for the direct observation of low mass stars and brown dwarfs in their natal environments. In other words, the observed mass distribution of a young cluster *is* its IMF.

In this paper we present results from FLAMINGOS photometry and spectroscopy of the young cluster NGC 2024, including a new age and IMF for the cluster. NGC 2024 is a young (< 1 Myr) HII region which remains deeply embedded in its parent molecular cloud (L1630, also known as Orion B). Distance estimates for the Orion B cloud range from 360-480 pc (Anthony-Twarog 1982; Brown et al. 1994), with the distance to the subgroup containing NGC 2024 estimated at 415pc (Anthony-Twarog 1982). Infrared photometric studies of low mass objects in the region indicate that the star formation efficiency is high (20-40%) and the majority of detected objects exhibit near-infrared excess emission indicative of hot circumstellar material (Lada et al. 1991; Comeron et al. 1996; Haisch et al. 2000). The proximity, extreme youth, and indicators of active star formation in NGC 2024 combine to make this an ideal region to study brown dwarf formation.

2. OBSERVATIONS AND DATA REDUCTION

All imaging and spectroscopic data included in this work were taken using the Florida Multi-Object Imaging Near-Infrared Grism Observational Spectrometer (FLAMINGOS, Elston 1998) mounted on the Kitt Peak National Observatory (KPNO) 2.1m and 4m telescopes as part of the FLAMINGOS giant molecular cloud survey⁴. FLAMINGOS employs a 2048×2048 HgCdTe HAWAII-2 infrared array with 18 micron pixels. On the KPNO 4m telescope this corresponds to a plate scale of $0.318''/\text{pixel}$ and a $10.8' \times 10.8'$ field of view. On the KPNO 2.1m telescope, the plate scale is $0.608''/\text{pixel}$, yielding a field of view of $20.5' \times 20.5'$. The details of both the imaging and spectral data acquisition and reduction are discussed in the following sections.

⁴ NAO Survey Program 2000B-0028: *Towards a Complete Near-Infrared Spectroscopic Survey of Giant Molecular Clouds* (PI: E. Lada)

¹ email: levine@astro.ufl.edu

² Current Address: Department of Physics and Astronomy, SUNY Geneseo, One College Circle, Geneseo, NY 14454

³ Deceased

2.1. FLAMINGOS Imaging and Photometry

J , H , and K -band images of NGC 2024 were obtained on 2001 November 19 using FLAMINGOS on the KPNO 4m telescope. The data were taken using a 16-point dither pattern with individual exposure times of 60s for J and H and 30s for K , yielding total exposure times of 16 minutes in J and H and 8 minutes in K . Typical seeing at all wavelengths was $1''.1$ - $1''.2$ FWHM.

The imaging data were reduced and photometered using the FLAMINGOS data reduction and analysis pipelines within IRAF. Briefly, the data reduction pipeline includes linearization of all data, dark subtraction and division by a normalized flat field, a two-pass sky subtraction routine, removal of bad pixels and finally image resampling and median combination of individual frames. The analysis pipeline incorporates source detection and extraction, aperture and point spread function (PSF) photometry with a 2nd order variable PSF, astrometry, photometric calibration against 2MASS, and the combination of multi-wavelength data into a single catalog. It should be noted that some small misalignments and/or fabrication errors in the FLAMINGOS optical system cause some noticeable PSF degradation which is more pronounced at larger field positions. In addition, images centered on NGC 2024 have a strong nebular contribution to the background which is difficult to remove with simple aperture photometry. PSF photometry is better able to handle these variations thus we present only PSF photometry for the remainder of this work.

Photometric quality was assessed using a direct comparison between FLAMINGOS photometry and the 2MASS database. The 1σ scatter in each magnitude bin was calculated down to the 2MASS completeness limits of $J < 15.8$, $H < 15.1$ and $K_s < 14.3$ (Cutri et al. 2003), and the results were combined using a weighted average with the weights dependent on the number of sources in each bin. In regions with little to no nebular emission, we estimate the bulk of our photometry is accurate to within 0.03 magnitudes. The 5σ detection limits in these regions are $J=20.1$, $H=19.5$, and $K=18.5$. For regions with large amounts of nebula, as in the center of NGC 2024, the scatter with respect to 2MASS is much larger (~ 0.15 magnitudes) than that expected from purely photometric noise. A similar effect has been noted by other authors studying young clusters with significant nebular emission (e.g. Muench et al. 2003 in IC 348 and Muench et al. 2002 and Slesnick et al. 2004 in the Trapezium) and is usually attributed to the large size of the 2MASS pixels ($\sim 2.0''$), intrinsic variability of young objects, and variations in aperture size coupled with the strong nebular background. The photometric scatter with respect to 2MASS was also larger for objects on the edge of detector where the data rapidly degrade due to a delamination of the engineering array. For objects in this region (generally non-nebular), we used photometry taken from the FLAMINGOS/KPNO 2.1m Orion B imaging survey, taken on 2001 December 18 and reduced in the manner described above. Sources having 2.1m photometry are identified in Table 3 and estimated to have photometric accuracy within 0.04-0.05 magnitudes which is typical of FLAMINGOS fields observed during the 2001-2002 observing season (C. G. Román-Zúñiga et al. 2006, in preparation).

2.2. Spectroscopic Sample Selection

The majority of spectroscopic targets presented in this study were observed on the KPNO 4m telescope. Target selec-

tion for 4m spectroscopy of NGC 2024 was accomplished via the following procedure: First, brown dwarf candidates were selected by comparing their positions in an $H/H-K$ color-magnitude diagram (left panel of Figure 1) with the 0.3 Myr isochrone of D'Antona & Mazzitelli (1997) and choosing sources located below a reddening vector extending from $0.08 M_{\odot}$. Additional young sources were selected by targeting objects which exhibited an infrared excess (IRX) in the $J-H$ vs $H-K$ color-color diagram (right panel of Figure 1). Finally, once a slit mask was designed to target a maximum of IRX sources or brown dwarf candidates, the remaining spaces on the mask were filled with all available objects having K magnitudes brighter than 15.0 for plates taken after December 2003 and brighter than 16.5 for plates taken earlier, irrespective of their IRX or brown dwarf candidate status. In this manner, we targeted 120 unique sources on five slit masks. The spatial distribution of 4m targets can be seen in Figure 2.

A handful of brighter sources ($K < 13.0$) in the region depicted in Figure 2 were targeted for observation on the 2.1m telescope as part of a larger survey to characterize the stellar population of NGC 2024. These sources (indicated with squares in the figure) were selected solely on the basis of their IRX status and K magnitudes. Although this sample is likely dominated by earlier spectral types, we include these sources since any classifiable M stars in the set will aid in determining the age of the low mass cluster population.

It should be noted that the photometric catalog luminosity functions turn over at 18.75, 18.5, and 17.5 mag for J , H , and K respectively. These turnovers can be interpreted as representative completeness limits, thus we are confident that our photometry is complete well beyond the $K=16.5$ targeted limit of the spectroscopic survey.

2.3. FLAMINGOS Spectroscopy

2.3.1. 4m Data Acquisition

FLAMINGOS spectra of the sources selected above were taken through five different slit masks using the KPNO 4m telescope on the nights of 2003 January 19, 2003 December 06, 2003 December 10 and 2004 December 01. Each slitlet had a width of 3 pixels ($0''.95$) resulting in a resolving power of $R \sim 1300$. Sources were observed using the JH filter (0.9 - $1.8 \mu\text{m}$) coupled with the JH grism, providing complete spectral coverage in both the J and H bands simultaneously.

For each mask, 300s exposures were taken in sets of four, dithering between two positions on the chip in a standard ABBA pattern. The separation between positions A and B was $4''$ along the long dimension of the slitlets. Total exposure times for each slit mask ranged from 40-65 minutes and are detailed in Table 1. Short exposure, long slit spectra of a nearby G dwarf were taken immediately following the science observations to correct for telluric absorption. Quartz lamp flat fields and HeNeAr arc lamp spectra for wavelength calibration were also obtained for all targets.

2.3.2. 2.1m Data Acquisition

Spectra of the brighter targets were obtained with FLAMINGOS on the KPNO 2.1m telescope on the night of 2003 November 29. Each slitlet had a width of 3 pixels ($1''.82$) again resulting in a spectral resolution of $R \sim 1300$. All sources were observed using the combination of the JH filter and the JH grism with 300s exposures taken in sets of 4, yielding a total exposure time of 70 minutes. Flat fields were taken using an illuminated white screen mounted on the inside

of the telescope dome and wavelength calibration was determined using the atmospheric OH emission lines intrinsic to all NIR spectra. Finally, a nearby G0 star was observed to correct for telluric absorption.

2.3.3. Data Reduction

All FLAMINGOS spectra taken for this study (both 2.1m and 4m data) were reduced using a combination of standard IRAF procedures and custom FLAMINGOS routines. We determined that a linearization correction was not necessary as the correction was $<1\%$ of the raw flux levels for usable data and the high order correction needed would likely introduce larger errors. Consequently, the raw data were first dark subtracted and subsequently divided by a normalized flat field created by averaging a number of dark subtracted quartz flats. A pairwise subtraction of adjacent exposures was then employed to remove background sky emission. The sky subtracted images were aligned and combined using *imcombine* to create a single image containing all spectra for each slit mask or standard star.

Long slit spectra were extracted in a straightforward manner, using the IRAF task *apall*. The dispersion correction for the long slit data was derived from similarly extracted arc lamp spectra as the background OH emission lines were not bright enough due to the short exposure times used for the standards. Extraction of the multi-slit data was accomplished by first cutting a two-dimensional image of each slitlet from the final combined image described above. Each aperture was then traced and extracted separately using *apall*. The dispersion solutions for multi-slit data were derived using background OH emission lines local to each slitlet. Once the wavelength calibration was applied target spectra were divided by the G dwarf spectrum to correct for atmospheric absorption. Features introduced by the standard star division were removed by multiplying the resultant spectra by the solar spectrum. Finally, all corrected spectra were smoothed to a resolution $R \sim 500$ and normalized so that their flux values at $1.68 \mu\text{m}$ were unity. Note that because we are using a visual classification process based on broad absorption profiles (§3.1) we are not losing any critical information by lowering the resolution – rather, the increase in S/N makes the overall shape easier to discern, facilitating spectral classification.

In this manner, we were able to extract 111 individual spectra from the 4m data and 11 spectra from the 2.1m data set. Sources which were not extracted were either too faint to allow for an accurate aperture trace or located at the top or bottom edge of the detector where the quality of the flat field rapidly degraded.

3. SPECTRAL CLASSIFICATION

3.1. Spectral Types

In order to properly classify objects in our NGC 2024 sample, it is necessary to compare the spectra of program sources with spectra of objects with known spectral types. The most prominent features in low resolution infrared spectra of late-type objects are the narrow atomic lines of H I and Mg I, which decrease in strength for later objects, and broad water absorption bands which become stronger as effective temperatures decrease. The water absorption bands are ideal for classifying young objects (Wilking et al. 1999; Reid et al. 2001; Slesnick et al. 2004) as they produce a very distinct continuum shape which becomes even more pronounced for later spectral types, even at very low spectral resolutions. However,

steam absorption is significantly stronger in the NIR spectra of young objects than in field dwarfs of the same optical spectral type (Lucas et al. 2001; McGovern et al. 2004). Consequently, if we use field dwarf standards to type our NGC 2024 members, the derived spectral types will be systematically too late. Rather, we must use optically classified young objects to make an accurate comparison.

Due to the dearth of published spectral types for late-type objects in NGC 2024, we turned to the nearby, young IC 348 cluster in Perseus. IC 348 has been extremely well studied by multiple authors (e.g. Luhman et al. 2003b; Muench et al. 2003 and references therein) and contains a number of known members with established optical classifications. Further, the youth of the cluster (mean age ~ 2 Myr, Herbig 1998) implies that spectral template stars taken from IC 348 membership lists will be similar in age and surface gravity to our NGC 2024 program objects (see §3.2 for further discussion of surface gravity effects). Table 2 lists the identifications, positions, and spectral types of the IC 348 standards as taken from Luhman et al. (2003b). FLAMINGOS spectra of these standards were obtained and reduced as part of a parallel survey to classify new members of IC 348 Luhman et al. (2005a, hereafter L05). In addition, we also obtained a spectrum of the young Taurus member KPNO-Tau 4 to provide a very late type template (M9.5, Briceño et al. 2002).

Spectral types for candidate members of NGC 2024 were determined by visually comparing our program spectra with FLAMINGOS spectra of the IC 348/Taurus standards, following the procedure described in L05. In brief, spectra were first forcibly “dereddened” to yield a uniform continuum slope for all objects (including standards). This was accomplished by normalizing all spectra so that the flux at $1.68 \mu\text{m}$ had a value of 1.0. We then used the IRAF *deredden* task to redden or deredden the spectra until the flux value at $1.32 \mu\text{m}$ matched the flux of the standards (flux=1.21). The points at 1.32 and $1.68 \mu\text{m}$ were chosen because they represent the regions least affected by the stellar absorption features. A spectral type for each object was then determined by visually comparing the strength of the broad band water absorption features to those of the standards. The major advantage to this visual method of classification is that it is independent of the actual reddening of the objects in question.

When classifying spectra, particular attention was paid to the slope and depth of the J-band fall-off at $1.35 \mu\text{m}$, the strong absorption features in the H-band on either side of $1.68 \mu\text{m}$, and the strength of the Mg I line. Classifications were fine-tuned by placing all spectra in order of increasing spectral type and adjusting the sequence to ensure that the strength of the water absorption monotonically increased with spectral type. We estimate this method to be quite robust, with typical errors in spectral type of ± 0.5 -1 subclasses. A selection of both candidate and standard spectra are shown in Figure 3 with the strongest atomic and molecular features marked. Objects with spectral types $< M6$ are plotted with $R \sim 500$ and objects with spectral types $\geq M6$ have been further smoothed to $R \sim 200$ to aid in the classification process.

The final classifications yielded 65 unique objects from the 4m sample with identifiable M type spectra (ranging from M1 to $> M8$) and 2 sources with spectral types earlier than M0. In addition, we also extracted 4 duplicate sources which when independently classified yielded spectral types in agreement with the original source to within 0.25 subclasses. Of the ~ 40 4m extracted objects which were not classified, 14 were filler targets with K magnitudes > 15.0 which we have learned are

typically too faint to classify with our current exposure times. The remaining unclassified sources while bright at K , were typically highly reddened objects with poor signal to noise in the J and H bands after dereddening. The 2.1m sample yielded 4 new M type objects and one duplicate classification (which agreed with the 4m source to within 0.5 subclasses).

3.2. Surface Gravity

Many of the atomic and molecular features commonly found in the NIR spectra of M stars are sensitive to surface gravity (Gorlova et al. 2003; McGovern et al. 2004). This sensitivity provides a natural method for distinguishing young sources (which have intermediate surface gravities) from relatively high surface gravity field dwarfs or low gravity background giants. In this section we describe the most prominent low resolution ($R \sim 500$) surface gravity indicators and discuss their implications for our data.

Figure 4 shows the progression of the strongest gravity sensitive features visible in our data—the broad water absorption features in both the J and H bands and a narrow potassium doublet at $1.243/1.252 \mu\text{m}$ —as a function of both surface gravity and spectral type. For the M3 objects both the J and H -band H_2O induced fall-offs are steepest for the young star. This effect becomes more dramatic for the M6 and M9 objects where the field dwarf continuum profiles have broad H -band plateaus versus a distinct triangular shape for the young objects. (The same effect was also noted by Lucas et al. (2001) and L05). Looking at the M6 and M9.5 objects, the field stars have a strong potassium doublet which is weak or absent in the lower gravity atmospheres of the young stars and giant. Finally, it is also apparent that the two giants have a flatter continuum profile and a much higher frequency of H -band absorption lines. Consultation of the literature (e.g. the low resolution infrared spectral libraries of Lancon & Rocca-Volmerange (1992)) confirms that this is a hallmark of giant stars and is likely caused by overtones of CO and OH as well as blended molecular lines only visible at low surface gravities.

Applying the above diagnostics to our data we note that the majority of sources display the distinct triangular continuum profiles indicative of youth. We also find that the J -band potassium lines are absent from our spectra therefore we are confident that there are no field dwarfs present in the sample. Two sources (60 and 64) display enhanced absorption in the H -band and may be background M giants. These are noted in Table 3.

3.3. Infrared Excess Emission

The presence of excess flux in the near infrared is commonly taken to be an indicator of thermal emission by warm dust in a circumstellar disk. This type of emission can result in the weakening or *veiling* of both narrow and broad-band spectral lines. If the amount of veiling is significant, it can affect spectral classification causing an object to appear earlier than its true spectral type. In this section we attempt to quantify the effect of veiling on our classification process by visually inspecting our sample and examining its infrared excess (IRX) properties.

Visual inspection of the spectra yielded one object (source 5, M1.75) with obviously weak Mg I absorption likely caused by veiling. In addition, excluding the possible giants (see above), 27 out of 67 objects or $40\% \pm 9\%$ of our classified M star sample exhibit an IRX as determined via a comparison of each object’s expected intrinsic $H - K$ color (inferred

from spectral type) with its dereddened observed $H - K$ color. (The reader is referred to §4.1 for an explanation of intrinsic color choice and dereddening methods.) What fraction of IRX sources can be expected to have significant veiling? To answer this question we have calculated r_k , the K -band veiling index for each source.⁵ The typical errors on r_k are ± 0.08 magnitudes, implying that we should not place too much weight on individual values of r_k which are close to zero. However, since the primary purpose of this r_k analysis is to identify the sources with veiling strong enough to bias our spectral classification, this error is acceptable. As can be seen from Table 3, only source 38 ($r_k=0.62$) exhibits an amount of veiling near $r_k=0.6$, the median value for Classical T Tauri stars (Meyer et al. 1997). Consequently, we note the potential bias towards an earlier spectral type for this object.

4. H-R DIAGRAM

In order to construct an IMF for NGC 2024, we must determine the mass distribution of objects in our sample. In this section we combine spectral types and infrared photometry to derive visual extinctions, effective temperatures and bolometric luminosities for our objects. We then place these data on the H - R diagram and use theoretical PMS evolutionary models to infer masses and ages for the sample.

4.1. Extinction

Because NGC 2024 is so deeply embedded in its natal cloud, there is a large and variable amount of extinction in the region which acts to differentially redden source magnitudes. In order to properly estimate physical parameters and infer masses and ages, this reddening must be accounted for. The amount of extinction towards a given source is typically derived by dereddening its broadband colors, however, care must be taken when choosing passbands. The redder infrared bands are less sensitive to variations in extinction but may also be contaminated by infrared excess emission arising from a circumstellar disk. Optical bands suffer from contamination due to UV excess emission from the stellar photosphere. It is generally agreed upon that bands between R and J are most sensitive to extinction while minimizing the effects of excess emission (*cf.* Meyer et al. 1997; Luhman et al. 2003b). As we do not have reliable optical photometry for NGC 2024, we elected to use our bluest infrared bands to derive extinction estimates for each source.

Extinction estimates were determined by comparing our observed $J - H$ colors with the empirically determined intrinsic M dwarf colors of Leggett (1992); Leggett et al. (1996) and Dahn et al. (2002) and then converting the color excess to an A_V measurement using the reddening law of Cohen et al. (1981). The choice of both the intrinsic colors and the reddening law was based primarily on photometric system. FLAMINGOS filters closely approximate the CIT system (Elston et al. (2003) and the FLAMINGOS web pages) thus we opted for a reddening law and intrinsic color set derived in the same system. We opted against using theoretical PMS colors since at young ages these are highly dependent on model input physics. For the one source lacking J -band photometry, an extinction estimate was derived using $H - K$ colors. It should be noted that for comparison we also estimated visual

⁵ The veiling index r_λ is defined as $F_{\lambda_{ex}}/F_{\lambda_*}$. Converting to photometric K -band excess yields $r_k = [(1+r_H)10^{((H-K)-(H-K)_0-0.065A_V)/2.5} - 1]$. Note that because we are dereddening to intrinsic dwarf colors our values for r_k are lower limits since r_b is assumed to be zero (Meyer et al. 1997).

extinctions for all sources using $H-K$ intrinsic colors and by dereddening objects to a model isochrone in both $J/J-H$ and $H/H-K$ color magnitude diagrams. These methods yielded A_V values which deviated from the $J-H$ intrinsic color estimates by as much as 1-2 magnitudes for $J/J-H$ and 3-4 magnitudes for $H/H-K$. Effects of this deviation will be discussed in §§4.2 and 5.2.

Figure 5 shows the distribution of visual extinctions derived from $J-H$ intrinsic colors. Values range from $\sim 1-30$ visual magnitudes with a mean A_V of 10.7 magnitudes. This is in good agreement with the survey of Haisch et al. (2000), who find a range of A_V from roughly 0-30 visual magnitudes and a mean A_V of 10.4.

4.2. Effective Temperatures and Bolometric Luminosities

Spectral types were converted to effective temperatures using a linear fit to the adopted temperature scale of Luhman et al. 2003. This temperature scale, derived from the young quadruple system GG Tau, falls between dwarf and giant temperature scales and is thus appropriate for the intermediate surface gravity objects studied here. Absolute magnitudes were calculated by dereddening K magnitudes (see below) using the A_V derived in §4.1 and applying a distance modulus of 8.09 (Anthony-Twarog 1982). Bolometric magnitudes and luminosities were derived using the bolometric corrections of Leggett (1992); Leggett et al. (1996) and Dahn et al. (2002) as they were observationally determined using CIT photometry.

While J -band is typically the preferred wavelength for deriving bolometric luminosities as contaminating excess effects are minimized (Luhman 1999, see also §4.1), we have elected to use the K -band since luminosities derived from K magnitudes are far less sensitive to errors in dereddening. As discussed above, photometrically derived extinction values can have errors as large as 3-4 magnitudes. A change in A_V of 3 magnitudes corresponds to nearly a magnitude of uncertainty in dereddened J -band magnitudes but yields a much smaller ΔK (< 0.3 mag). Although K magnitudes are more sensitive to excess emission from a warm circumstellar disk, this effect is small in log-Luminosity space (average $\Delta \log L \sim 0.06$ dex). Even when combined with the A_V uncertainty, the net uncertainty in K -derived bolometric luminosities (± 0.17 dex) remains smaller than the corresponding uncertainty using J -band to derive bolometric luminosities (± 0.32 dex).

4.3. Masses and Ages

In order to derive mass and age estimates for young sources we must place the sources on an H-R diagram and compare them with pre-main sequence evolutionary models. The most frequently used models for low mass stars and high mass brown dwarfs (rather than planetary mass objects) are those of D’Antona & Mazzitelli (1997, hereafter DM97) and Baraffe et al. (1998, hereafter BCAH98). The primary differences between these two models are their treatment of convection (mixing-length theory for BCAH98 and full spectrum turbulence for DM97) and the assumption of grey atmospheres in DM97 vs. non-grey in BCAH98. BCAH98 and references therein argue that the grey atmosphere approximation is inappropriate for stars whose effective temperatures fall below $\sim 4500-5000$ K as molecules present in the atmospheres will introduce strong non-grey effects. There is some evidence supporting this claim as both White et al. (1999) and Luhman et al. (2003b) used empirical isochrones defined with low mass members of IC 348 and Taurus and the young

quadruple system GG TAU to show that the BCAH98 models agree better with observational constraints. Consequently, while we present H-R diagrams using both sets of tracks, for the remaining discussion we will focus primarily on results derived from the BCAH98 models.

Figure 6 shows H-R diagrams for our classified sources in NGC 2024 along with the PMS evolutionary models of D’Antona & Mazzitelli (1997) and Baraffe et al. (1998). The triangular points represent 2.1m classifications and sources with diamonds were classified using 4m spectra. The two asterixes represent the possible background giants (see §4). Individual object data are tabulated in Table 3. Two typical error bars for an M5 dwarf are shown in the lower left corner. The solid line was derived by classically propagating the measured errors in the photometry, spectral type, and distance modulus. In this case, the error in luminosity is dominated by error in the distance to NGC 2024. The dashed line incorporates an additional error of ± 3 magnitudes (corresponding to ± 0.2 dex) in the reddening estimate (refer to §4.1) which dominates the error bar and leads to a larger uncertainty in the calculated luminosity.

Mass and age estimates were derived from the BCAH98 models by interpolating between the isochrones and mass tracks shown in Figure 6. Sources falling above the youngest isochrone (1 Myr) were assumed to have an age < 1 Myr and were dropped down to the 1 Myr isochrone along a line of constant effective temperature to derive a mass estimate. In this manner we derived masses spanning a range from 0.02 to $0.72 M_{\odot}$ (with 23 objects falling below $0.08 M_{\odot}$) and ages ranging from < 1 to ~ 30 Myr.

5. PROPERTIES OF NGC 2024

5.1. Cluster Membership

Prior to drawing any conclusions regarding the age of NGC 2024 or its substellar population, it is necessary to evaluate the membership status of sources in our sample. In the absence of proper motion data, we must rely on other diagnostics to determine whether objects are bona fide cluster members or foreground or background sources projected on the cluster area. The discussion of surface gravity effects in §3.2 rules out foreground or background dwarf contamination in our spectroscopic sample as there are no potassium lines present in our spectra. In addition, NGC 2024 is deeply embedded in a core of dense gas (Lada et al. 1991; Lada et al. 1997) which will obscure background field stars, limiting the number of field contaminants in the photometric sample. The average column density of hydrogen in a 0.6 pc clump centered on NGC 2024 has been estimated from $C^{18}O$ emission to be $N(H_2) = 4.6 \times 10^{22} \text{ cm}^{-2}$ (Aoyama et al. 2001). Given that a molecular hydrogen column density of 10^{21} cm^{-2} corresponds to 1 magnitude of visual extinction (Bohlin et al. 1978), background sources in this region will be viewed through 46 magnitudes of visual extinction, or ~ 4.1 magnitudes of K -band extinction. The spectroscopic sample includes sources down to $K \simeq 15$. Background objects contaminating this sample are seen through the cloud and thus will have unreddened magnitudes $K \leq 11$. Looking at the distribution of sources in an off-cloud FLAMINGOS control field as well as a similar area from the 2MASS database, we estimate that there are no more than 5 background sources with $K \leq 11$. As this is a relatively insignificant contribution to the total photometric KLF, we conclude that a background correction is unnecessary. We do note the possibility of giant contamination for two spectroscopic sources (60 and 64) which display enhanced absorp-

tion in the H-band and we exclude these objects from further analysis.

5.2. Age of NGC 2024

Sources in the H-R diagrams in Figure 6 do not fall along a single isochrone but rather show a scatter in age ranging from $\ll 1$ Myr to ~ 30 Myr, irrespective of the PMS models used. This type of width in the evolutionary sequence of young clusters is common and is usually attributed to a variety of effects including: real age differences between sources, errors in luminosity derived from uncertainties in the derived reddening, photometric uncertainty (these effects are represented by the error bars in the figure), as well as distance variations between sources, variability due to accretion and rotation of young objects, and unresolved binaries. The median age of the entire sample however should be representative of the median age of the cluster population in the mass range detected here.

Using the models of BCAH98 the majority of sources fall above the 1 Myr isochrone. Consequently, the median age of the cluster can only be constrained to < 1 Myr. However, the DM97 models extend to younger ages than those of BCAH98. Even though we have elected to place more weight on results derived with the BCAH98 models (see §4.3), the DM97 models provide us with additional information on the age of the cluster population as well as a means to compare our results with previous surveys of NGC 2024 and other regions where authors have used the DM97 models to derive an age. Using the DM97 models we derive a median age of 0.5 Myr. If we factor in errors in the distance modulus (8.09 ± 0.17 , Anthony-Twarog 1982), this leads to a possible age range of 0.4-0.6 Myr. Including a 3 magnitude shift in reddening (refer to §4.1) yields a larger range of 0.2-0.9 Myr. All of these results remain consistent with the age derived from the BCAH98 models, placing NGC 2024 at < 1 Myr.

Our derived age of 0.5 Myr for NGC 2024 is in good agreement with ages found by previous surveys of NGC 2024. Both Meyer (1996, hereafter M96) and Ali et al. (1998) used infrared photometry and spectroscopy with the models of D’Antona & Mazzitelli (1997) to derive mean ages of 0.3 and 0.5 Myr respectively. Further, M96 used a distance modulus of 8.36 magnitudes. Increasing the distance to the cluster acts to increase the derived bolometric luminosity of sources, making objects appear younger. Indeed, if we use the larger distance modulus with the models of DM97, we derive a median age of 0.3 Myr which is in excellent agreement with the results of M96.

A few sources in our H-R diagrams appear to have ages which deviate significantly from the median. Using either set of PMS models there is a small, lower luminosity population with inferred ages > 3 Myr. In order to attribute these low luminosities to general scatter caused by photometric errors and uncertainties introduced by variability (generally no more than ± 0.2 mag at K), derived reddening (± 0.3 mag, see above), and distance modulus (± 0.2 mag), these effects would have to combine to produce at least a 1-2 magnitude shift at K . On the other hand, it has been noted by multiple authors (e.g. Luhman et al. 2003b; Slesnick et al. 2004; Wilking et al. 2004) that a circumstellar disk can act to occult the central source, resulting in an underestimate of the object’s luminosity and thus an overestimate of the object’s age. We have examined the infrared excess properties of the subsample in question and indeed, irrespective of the model isochrones used, all but one of the objects with an inferred age > 3 Myr have excess flux, indicating the presence of circum-

stellar material.

Looking at Figure 6, we also notice that object age may be slightly mass dependent with the less massive sources appearing younger. To quantify this trend, we have divided our sample into two populations: objects with masses lower than the median mass and objects with masses higher than the median mass ($M_{median} \simeq 0.15 M_{\odot}$). Using the BCAH98 models we are unable to detect an age difference between the low and high mass samples as both have median ages < 1 Myr. However, the median ages indicated by the DM97 models are somewhat different from one population to the other. The low mass sample has an age of 0.3 Myr and the higher mass sample has an age of 0.9 Myr. There are a number of possible explanations for this effect. First, the trend may be an artifact arising from uncertainties in the evolutionary models at very young ages and low masses. No two sets of PMS tracks look alike in the brown dwarf regime thus it is a distinct possibility that the apparent age segregation is caused by a problem with the tracks. On the other hand, the observed mass dependence could be a selection effect caused by the intrinsic faintness of the older substellar population – according to the BCAH98 models even the highest mass brown dwarfs will be undetectable by our survey by the time they reach ages of 2-3 Myr and this limit becomes younger for lower mass objects. Finally, it is also possible that this effect is real. If so, this may be evidence for sequential formation as a function of mass where lower mass objects form later in the evolutionary sequence of a young cluster. Unfortunately, our data are not sensitive enough to distinguish between these possibilities – deeper spectroscopic observations are needed.

5.3. The Substellar Population

5.3.1. Spatial Distribution of Sources

Figure 7 presents the spatial distribution of all sources classified using FLAMINGOS spectra. Open circles are objects with $M > 0.08 M_{\odot}$, filled triangles have masses $M < 0.08 M_{\odot}$, and asterixes are the possible giants. The star at the center of the cluster represents IRS2b, the likely ionizing source for the region (see below). It can be seen from this figure that the substellar objects are not localized to one region but rather appear to be distributed similarly to the stellar mass objects classified here. It should be noted that the dearth of classified objects (either stellar or substellar) in the center of the cluster is a selection effect caused by the high extinction in this region blocking much of the J and H -band flux.

5.3.2. Disk Frequency

As discussed in §3.3, the presence of an infrared excess is commonly taken to be an indicator of thermal emission from a circumstellar disk. Disks around brown dwarfs are of particular interest because their presence or absence has implications for the likelihood of planet formation (planets form within circumstellar dust disks) and the formation mechanism of brown dwarfs (accretion disks play an important role in the star formation process). Combining our spectral classifications with $H-K$ intrinsic colors we find $40\% \pm 9\%$ of sources in our total sample have an $H-K$ color excess. This method of selecting excess sources has been shown by Liu et al. (2003) to be more sensitive to small IR excesses (as opposed to the traditional JHK color-color diagrams) and is thus well suited for investigating the disk properties of brown dwarfs, which are expected to have smaller excesses than their stellar counterparts. Approximately one third of the excess sources detected using

the color-spectral type analysis have masses which place them below the hydrogen-burning limit (spectral types $\geq M6$). This yields a substellar HK excess fraction for NGC 2024 of 9/23 or $39\% \pm 15\%$, where quoted errors are derived from Poisson statistics.

Substellar excess fractions have been compiled for a number of other regions. For example, Muench et al. (2001) used JHK color-color diagrams to examine a set of photometrically selected brown dwarfs in the Trapezium cluster and found a substellar excess fraction of $\sim 65\% \pm 15\%$. In a follow-up L' study of the same region, Lada et al. (2004) find a $K-L'$ excess fraction of $52 \pm 20\%$ for their spectroscopically selected brown dwarf sample and 67% using a $JHKL$ color-color analysis for the larger photometric sample. More recently, Luhman et al. (2005b) used the Spitzer Space Telescope to obtain mid-infrared photometry for low mass members of the IC 348 and Chamaeleon I clusters, finding that $42\% \pm 13\%$ of brown dwarfs in IC 348 and $50\% \pm 17\%$ of brown dwarfs in Chamaeleon exhibit excess emission, consistent with our result for NGC 2024.

Based on the above results (placing more emphasis on studies with spectroscopic information), we can conclude that 40-50% of brown dwarfs are surrounded by circum(sub)stellar disks. Note though in many cases the quoted substellar excess fractions are deemed lower limits to the true substellar disk fraction (e.g. Lada et al. 2004; Luhman et al. 2005b). This is also true for NGC 2024. Disk modeling by Liu et al. (2003) shows that the *maximum* expected K -band excess for a disk with no inner hole is 0.42 magnitudes for an M6 dwarf and 0.31 magnitudes for an object classified as M9. However, the L' observations of Liu et al. (2003) are more consistent with disks having an inner hole $R_{in} \approx (2-3)R_*$. The K -band excess for these objects would be very small or undetectable using the $H-K$ analysis we present here.

Our choice of intrinsic colors may also lead to an underestimate of the substellar disk fraction in NGC 2024. We have used an intrinsic color set derived from observations of field dwarfs. Our targets are pre-main sequence objects which have lower surface gravities than field dwarfs (e.g. §3.2) and thus bluer $H-K$ intrinsic colors for a given spectral type (refer to the low surface gravity giant sequence plotted in Figure 1b as compared to the dwarf sequence plotted in the same figure). The assumption of the redder dwarf colors will preclude objects with a K -band excess similar to or smaller than the difference between PMS and dwarf colors from being counted as excess sources. Combining this effect with the fact that $H-K$ excess is a poor indicator of disk emission for substellar objects (see above), we conclude the true substellar disk fraction for NGC 2024 may be significantly higher than 39%. This yields further weight to the idea that the majority of brown dwarfs form through a disk accretion process similar to their stellar counterparts.

5.3.3. Low Mass IMF

Prior to constructing a mass function for NGC 2024, we must ensure that the subsample under consideration is representative of the overall cluster population. The left-hand panel of Figure 8 shows the uncorrected photometric luminosity function with the KLF of the final classified spectroscopic sample. Without placing any limits on the data, it can be seen that our spectroscopic survey is typically only 10-20% complete in the magnitude range from $K=10.5-15.0$. As discussed in §5.1, correcting for background field stars will have little effect. Rather, much of our incompleteness is caused by high

reddening within the molecular cloud itself (§4.1). Imposing an extinction limit on the data yields a higher completeness fraction and gives a more controlled sample from which we can construct an IMF. The right-hand panel of Figure 8 shows the K -band luminosity functions for all sources having $A_V \leq 15$ in both the photometric catalog and the final sample of classified objects. Disregarding the bins on either end (as they contain only one object each), it now appears that the spectroscopic KLF is a good representation of the total photometric KLF in the magnitude range $11.25 < K < 14.75$. Further, with the exception of the bin centered on $K=12.5$, the completeness fraction in the same magnitude range now extends from $\sim 25-60\%$ with a median value of 35%. Following the work of Slesnick et al. (2004), we corrected for this incompleteness by adding sources to each deficient magnitude bin according to the object mass distribution in that bin.

Figure 9 shows the spectroscopically derived mass function for NGC 2024. The solid line is the mass function for all objects with spectral types $\geq M0$, excluding the two possible giants (§5.1). Error bars are derived from Poisson statistics. The dashed line shows the IMF for the same sample corrected for the incomplete magnitude bins down to $K=14.75$. We estimate that for our extinction-limited sample, this corresponds to a mass completeness limit of $0.04 M_\odot$. The mass function rises to a peak at $\sim 0.2 M_\odot$ before declining across the stellar/substellar boundary. There is an apparent secondary peak around $\sim 0.03 M_\odot$ although the error bars are also consistent with a relatively flat IMF in this regime.

It should be noted that the exact shape of the substellar IMF is somewhat dependent on the choice of bin centers and sizes. For a bin width of 0.3 dex, shifting the bin centers in increments of 0.05 dex shifts the location of both the primary and secondary peaks through a range of masses from $\sim 0.25-0.1 M_\odot$ and $\sim 0.03-0.04 M_\odot$ respectively. Additionally, in some cases the secondary peak disappears and the substellar IMF becomes flat. Decreasing the bin width by 30% emphasizes the secondary peak, however, the errors remain consistent with a flat IMF. Increasing the bin widths by 30% either preserves the secondary peak, flattens the substellar mass function, or causes it to decline throughout the brown dwarf regime depending on the choice of bin centers.

6. DISCUSSION

The low mass IMF has been investigated for a number of other young star forming regions and in some cases the results are strikingly similar to the IMF derived here. For example, a variety of photometric and spectroscopic surveys have been completed in the extremely dense Trapezium cluster and the intermediate density IC 348 cluster by multiple authors (Hillenbrand & Carpenter 2000; Luhman et al. 2000; Muench et al. 2002; Luhman et al. 2003b; Muench et al. 2003; Slesnick et al. 2004; Lucas et al. 2005) and all find mass functions rising to a maximum at $\sim 0.1-0.2 M_\odot$ before declining into the brown dwarf regime, consistent with our NGC 2024 IMF peak at $\sim 0.2 M_\odot$. These results are very different from the mass function derived for the Taurus star forming region (characterized by its low gas and stellar densities) which peaks at $0.8 M_\odot$ (Briceño et al. 2002; Luhman et al. 2003a; Luhman 2004b). In addition, Muench et al. (2002) and Slesnick et al. (2004) cite a possible secondary peak in the Trapezium IMF below the hydrogen-burning limit although the locations of their respective peaks differ both from each other and our possible secondary peak ($\sim 0.05 M_\odot$ for Slesnick et al., $\sim 0.025 M_\odot$ for Muench et

al., as compared to $\sim 0.035 M_{\odot}$ for NGC 2024). If this peak is a real feature in the mass function it may indicate a break in formation mechanism for low mass objects (Muench et al. 2002). On the other hand, it may be an artifact introduced by the mass-luminosity relation for brown dwarfs and not a true reflection of the mass function itself (Muench et al. 2003). In addition, as discussed in §5.3.3, in the case of NGC 2024 the exact shape of the substellar mass function is influenced by binning thus the secondary peak may be a consequence of small number statistics and incompleteness below $0.04 M_{\odot}$.

A more robust tool for investigating the differences between low mass IMFs is the ratio of brown dwarfs to stars as this quantity is independent of the detailed structure and exact shape of cluster mass functions. Briceño et al. (2002) define the ratio of the numbers of stellar and substellar objects as

$$R_{ss} = \frac{N(0.02 \leq M/M_{\odot} \leq 0.08)}{N(0.08 < M/M_{\odot} \leq 10)}. \quad (1)$$

In our completeness corrected, extinction limited mass function for NGC 2024 there are 45 objects with masses $0.02M_{\odot} < M < 0.08M_{\odot}$ and 103 objects with masses $M > 0.08M_{\odot}$. In addition, there are 36 sources in our photometric catalog with K magnitudes brighter than the bright limit of our mass function ($K=11.25$, §5.3.3). Since the youngest (and thus brightest) object classified as substellar has a K magnitude of 11.75 with the majority of brown dwarfs falling below $K=12.75$ it is reasonable to infer that all of these bright photometric sources have masses greater than $0.08 M_{\odot}$. Finally, we include 9 sources from the 2MASS catalog with magnitudes brighter than the FLAMINGOS saturation limit which are also expected to be far more massive than the substellar limit. This yields a value of $R_{ss}=45/148$ or 0.30 ± 0.05 assuming Poisson errors.

The ratio of brown dwarfs to stars has been derived for a number of young star forming regions. In the Trapezium, Slesnick et al. (2004) find $R_{ss}=0.20$ which is slightly lower than the value of $R_{ss}=0.26 \pm 0.04$ found by Luhman et al. (2000). This variation in R_{ss} is likely caused by the use of different evolutionary models. Slesnick et al. (2004) employed DM97 tracks to derive masses whereas Luhman et al. (2000) used the BCAH98 models. We have recomputed the Trapezium R_{ss} using the data of Slesnick et al. (2004) with the BCAH98 models and find a higher value of $R_{ss}=0.30$, in excellent agreement with our result for NGC 2024. Similarly, looking at Figure 6 we note that had we chosen to employ the DM97 models we would have counted fewer brown dwarfs, leading to a lower value of R_{ss} in closer agreement with the result of Slesnick et al. (2004). To remain consistent in the ensuing discussion, however, from this point forward we will discuss only those values derived using the BCAH98 models.

Luhman et al. (2003b) use the BCAH98 models to compute R_{ss} for both the Taurus aggregates and the IC 348 cluster and find significantly lower R_{ss} values: $R_{ss}=0.14 \pm 0.04$ for Taurus and $R_{ss}=0.12 \pm 0.03$ for IC348. However, as surveys of Taurus have been expanded beyond the aggregate radii, the corresponding ratio of brown dwarfs to stars has also increased. Luhman (2004b) combined optical imaging and spectroscopy with infrared photometry from 2MASS to find $R_{ss}=0.18 \pm 0.04$ for a 12.4 deg^2 area. More recently, Guieu et al. (2006) completed an optical survey covering $\sim 28 \text{ deg}^2$, and find an updated R_{ss} for Taurus of 0.24 ± 0.05 . These results apparently bring the region into agreement with the Trapezium and (within the 1 sigma errors) NGC 2024, possibly indicating that brown dwarf formation occurs independent

of the local environment. On the other hand, both sets of authors note that their Taurus surveys may suffer from possible incompleteness at low stellar masses ($M=0.3-0.6M_{\odot}$, spectral types $\simeq M2-M4$). Further, Taurus is a very extended region ($> 100 \text{ deg}^2$) and both surveys, while significant do not yet have complete spatial coverage of the distributed population. Detections of additional low stellar mass objects by forthcoming surveys of Taurus may act to drive the R_{ss} values back down.

Guieu et al. (2006) also examined the dependence of R_{ss} on radial distance from the Taurus aggregates. They find that the number of brown dwarfs in the aggregate centers ($r < 0.7R_{agg}$, where R_{agg} is typically $0.5-1.1 \text{ pc}$) is depleted by a factor of 2.3 compared to the more extended population ($r \geq R_{agg}$). Guieu et al. (2006) conclude that this is best explained if brown dwarf formation is dominated by the embryo-ejection model (Reipurth & Clarke 2001) and the new brown dwarfs observed in the distributed Taurus population are ejected unbound objects that have dynamically evolved away from their birth sites. Unfortunately this model cannot explain the low value of R_{ss} in IC 348. According to the simulations of Kroupa & Bouvier (2003), the distance traveled by an ejected brown dwarf in time τ is inversely dependent on the size of the gravitational potential from which it escapes. The mass contained in the core of IC 348 ($\sim 100 M_{\odot}$ within 0.5 pc , Lada & Lada 1995) is significantly larger than the mass of a typical Taurus aggregate ($M < 50M_{\odot}$), however, their ages are similar (IC 348 and the distributed population of Taurus are both estimated to have $\tau \sim 2 \text{ myr}$). Consequently we can expect the ejected brown dwarf population in IC 348 to be contained within a radius smaller than the ejected population in Taurus. As mentioned above, R_{ss} in Taurus converges to 0.24 within $0.5-1.1 \text{ pc}$. Muench et al. (2003) investigated the radial dependence of the brown dwarf fraction in IC 348 on scales $0.5-1 \text{ pc}$ and find no increase in the number of brown dwarfs at large radii. In addition, the models of Kroupa & Bouvier (2003) predict that there can be at most 0.25 ± 0.04 brown dwarfs per star produced as ejected embryos. While formally consistent, this value remains slightly below the R_{ss} we find for NGC 2024, indicating a possible excess of brown dwarfs in the region. Clearly, a universal application of the embryo-ejection model as applied to Taurus cannot simultaneously explain the observed deficit of brown dwarfs in IC 348 and the possible excess of these objects in NGC 2024.

Another possibility is that the outcome of the brown dwarf formation process is not universal but depends on star forming environment. Briceño et al. (2002) and Luhman et al. (2003b) offer the explanation that the differences between the peak mass of the Taurus IMF and the young cluster IMFs may reflect a disparity among the local Jeans masses. There is some numerical evidence in support of this theory. Recent simulations of turbulent fragmentation by Padoan & Nordlund (2002, 2004) and Bate & Bonnell (2005) find that while the mass distribution for star forming cores appears to be independent of environment for masses larger than a solar mass, the shape of the mass function for subsolar masses is dependent on the gas density and local velocity dispersion. Specifically, for higher gas densities and velocity dispersions, the IMF peaks at lower masses and produces larger numbers of brown dwarfs. These results are in agreement with the higher IMF peak for Taurus as the average gas density in the region has been estimated to be orders of magnitude lower than that of IC 348, the Trapezium, or NGC 2024. However, simulations of turbulent fragmentation do not quite account for

the excess of brown dwarfs observed in the Trapezium and NGC 2024 ($R_{ss}=0.26$ and $R_{ss}=0.30$) R_{ss} as compared to IC 348 ($R_{ss}=0.12$).

An alternate formation mechanism has been put forth by a number of authors (e.g. Kroupa & Bouvier 2003; Whitworth & Zinnecker 2004; Robberto et al. 2004) who suggest that isolated brown dwarfs in young clusters can form when the accretion disk around a prestellar core is prematurely eroded by the strong ionizing radiation emitted from O and B stars. The ionizing source for NGC 2024 has recently been identified as IRS2b, a late O to early B main sequence star located in the core of the cluster (cf. Figure 7) and at the center of the radio continuum radiation field (Bik et al. 2003). The presence of an O star in NGC 2024, the detection of low accretion rates in the Trapezium (also in the presence of known O and B stars) (Robberto et al. 2004), and the absence of photoionizing stars in IC 348 indicates that photoevaporation of accretion disks may be a good explanation for the enhanced numbers of brown dwarfs in the Trapezium and NGC 2024. If this is the case, we would expect to observe a higher density of brown dwarfs in regions closest to the ionizing source(s). Unfortunately we do not have enough statistics in our current data set to test this theory, thus we defer further discussion to future work and simply note that while the IMF for solar to high mass stars appears uniform, the low mass end may depend on the local environment, particularly in young clusters where the preferred mechanism for brown dwarf formation may vary from region to region.

7. SUMMARY

We present FLAMINGOS photometry and spectroscopy for 71 low mass objects in NGC 2024. Water absorption features in low resolution *J* and *H* band spectra were used to find spectral types ranging from \sim M1 to $>$ M8 with typical errors in the classifications of 0.5-1 subclasses. A qualitative surface gravity analysis was used to distinguish cluster members from possible background giants. Spectral types for the 67 cluster members with M-type spectra were then converted to effective temperatures and photometry was used to calculate extinctions and bolometric luminosities for each source. Finally, objects were placed on H-R diagrams and masses and ages were inferred with the assistance of pre-main sequence evolutionary models.

We find a median age for NGC 2024 of 0.5 Myr using the

evolutionary models of D'Antona & Mazzitelli (1997), which is consistent with a median age <1 Myr as derived from the models of Baraffe et al. (1998). Derived masses range from $0.02 M_{\odot}$ to $0.72 M_{\odot}$ using the tracks of Baraffe et al. (1998), with 23 of the 67 objects falling below the stellar/substellar boundary. When looking at the spatial distribution of these objects, we find that rather than being relegated to one area of the cluster they appear to be evenly distributed relative to their stellar counterparts. Thirty nine percent of our classified brown dwarfs appear to have an infrared excess, possibly indicative of thermal emission from a warm disk. We define an extinction limited subsample of our spectroscopic sources and combine it with photometry to construct a mass function for the region. The IMF for NGC 2024 peaks at $\sim 0.2 M_{\odot}$, consistent with peak values found for the Trapezium and IC 348. The IMF then declines into the brown dwarf regime but exhibits a possible secondary peak around $0.035 M_{\odot}$. Finally, using this IMF we estimate the ratio of stellar to substellar objects in NGC 2024 to be $R_{ss}=0.30\pm 0.05$. This is consistent with, although slightly higher than the R_{ss} values found for the Trapezium cluster and the distributed Taurus population but roughly a factor of 2 higher than the R_{ss} found for IC 348. Taken together, these results may imply that the low mass end of the initial mass function is not universal but rather depends on the star formation environment.

We thank August Muench for many fruitful discussions and we are grateful to Kevin Luhman and the anonymous referee for their helpful comments on earlier versions of this manuscript. FLAMINGOS was designed and constructed by the IR instrumentation group (PI: R. Elston) at the University of Florida, Department of Astronomy with support from NSF grant (AST97-31180) and Kitt Peak National Observatory. The data presented in this work were collected under the NAO Survey Program, "Towards a Complete Near-Infrared Spectroscopic Survey of Giant Molecular Clouds" (PI: E. Lada) and supported by NSF grants, AST97-3367 and AST02-02976 to the University of Florida. This publication makes use of data products from the Two Micron All Sky Survey, which is a joint project of the University of Massachusetts and the Infrared Processing and Analysis Center/California Institute of Technology, funded by the National Aeronautics and Space Administration and the National Science Foundation.

REFERENCES

- Ali, B., Sellgren, K., Depoy, D. L., Carr, J. S., Gatley, I., Merrill, K. M., & Lada, E. 1998, *Astronomical Society of the Pacific Conference Series*, 154, 1663
- Anthony-Twarog, B. J. 1982, *AJ*, 87, 1213
- Aoyama, H., Mizuno, N., Yamamoto, H., Onishi, T., Mizuno, A., & Fukui, Y. 2001, *PASJ*, 53, 1053
- Baraffe, I., Chabrier, G., Allard, F., & Hauschildt, P. H. 1998, *A&A*, 337, 403
- Barrado y Navascués, D., Stauffer, J. R., Bouvier, J., Jayawardhana, R., & Cuillandre, J.-C. 2004, *ApJ*, 610, 1064
- Bate, M. R., & Bonnell, I. A. 2005, *MNRAS*, 356, 1201
- Bessell, M. S., & Brett, J. M. 1988, *PASP*, 100, 1134
- Bik, A., Lenorzer, A., Kaper, L., Comerón, F., Waters, L. B. F. M., de Koter, A., & Hanson, M. M. 2003, *A&A*, 404, 249
- Bohlin, R. C., Savage, B. D., & Drake, J. F. 1978, *ApJ*, 224, 132
- Bricenno, C., Luhman, K. L., Hartmann, L., Stauffer, J., & Kirkpatrick, J. D. 2002, *ApJ*, 580, 317
- Brown, A. G. A., de Geus, E. J., & de Zeeuw, P. T. 1994, *A&A*, 289, 101
- Burrows, A., Hubbard, W. B., Lunine, J. I., & Liebert, J. 2001, *Reviews of Modern Physics*, 73, 719
- Burrows, A., et al. 1997, *ApJ*, 491, 856
- Chabrier, G. 2002, *ApJ*, 567, 304.
- Cohen, J. G., Persson, S. E., Elias, J. H., & Frogel, J. A. 1981, *ApJ*, 249, 481
- Comeron, F., Rieke, G. H., & Rieke, M. J. 1996, *ApJ*, 473, 294
- Cutri, R. M., et al. 2003, *VizieR Online Data Catalog*, 2246, 0
- Dahn, C. C., et al. 2002, *AJ*, 124, 1170
- D'Antona, F., & Mazzitelli, I. 1997, *Memorie della Societa Astronomica Italiana*, 68, 807
- Delfosse, X., Tinney, C. G., Forveille, T., Epchtein, N., Borsenberger, J., Fouqué, P., Kimeswenger, S., & Tiphène, D. 1999, *A&AS*, 135, 41
- Elston, R. 1998, *Proc. SPIE*, 3354, 404
- Elston, R., Raines, S. N., Hanna, K. T., Hon, D. B., Julian, J., Horrobin, M., Harmer, C. F. W., & Epps, H. W. 2003, *Proc. SPIE*, 4841, 1611
- Gorlova, N. I., Meyer, M. R., Rieke, G. H., & Liebert, J. 2003, *ApJ*, 593, 1074
- Guieu, S., Dougados, C., Monin, J.-L., Magnier, E., Martín, E. L. 2006, *A&A*, in press (astro-ph/0509317)
- Haisch, K. E., Lada, E. A., & Lada, C. J. 2000, *AJ*, 120, 1396
- Herbig, G. H. 1998, *ApJ*, 497, 736
- Hillenbrand, L. A., & Carpenter, J. M. 2000, *ApJ*, 540, 236
- Kenyon, M. J., Jeffries, R. D., Naylor, T., Oliveira, J. M., & Maxted, P. F. L. 2005, *MNRAS*, 356, 89
- Kirkpatrick, J. D., et al. 1999, *ApJ*, 519, 802
- Kroupa, P., & Bouvier, J. 2003, *MNRAS*, 346, 369

- Kumar, S. S. 1963, *ApJ*, 137, 1121
- Lada, C. J., Muench, A. A., Lada, E. A., & Alves, J. F. 2004, *AJ*, 128, 1254
- Lada, E. A., Bally, J., & Stark, A. A. 1991, *ApJ*, 368, 432
- Lada, E. A., DePoy, E. L., Evans, N. J., & Gatley, I. 1991, *ApJ*, 371, 171
- Lada, E. A., Evans, N. J., & Falgarone, E. 1997, *ApJ*, 488, 286
- Lada, E. A., & Lada, C. J. 1995, *AJ*, 109, 1682
- Lancon, A., & Rocca-Volmerange, B. 1992, *A&AS*, 96, 593
- Leggett, S. K. 1992, *ApJS*, 82, 351
- Leggett, S. K., Allard, F., Berriman, G., Dahn, C. C., & Hauschildt, P. H. 1996, *ApJS*, 104, 117
- Liu, M. C., Najita, J., Tokunaga, A. T. 2003, *ApJ*, 585, 372
- Lucas, P. W., Roche, P. F., Allard, F., & Hauschildt, P. H. 2001, *MNRAS*, 326, 695
- Lucas, P. W., & Roche, P. F. 2000, *MNRAS*, 314, 858
- Lucas, P. W., Roche, P. F., & Tamura, M. 2005, *MNRAS*, 361, 211
- Luhman, K. L. 1999, *ApJ*, 525, 466
- Luhman, K. L. 2004, *ApJ*, 602, 816
- Luhman, K. L. 2004, *ApJ*, 617, 1216
- Luhman, K. L., Briceño, C., Stauffer, J. R., Hartmann, L., Barrado y Navascués, D., & Caldwell, N. 2003, *ApJ*, 590, 348
- Luhman, K. L., Lada, C. J., Hartmann, L., Muench, A. A., Megeath, S. T., Allen, L. E., Myers, P. C., Muzerolle, J., Young, E., Fazio, G. G. 2005, *ApJ*, 631, L69
- Luhman, K. L., Lada, E. A., Muench, A. A., & Elston, R. J. 2005, *ApJ*, 618, 810
- Luhman, K. L., Rieke, G. H., Young, E. T., Cotera, A. S., Chen, H., Rieke, M. J., Schneider, G., & Thompson, R. I. 2000, *ApJ*, 540, 1016
- Luhman, K. L., Stauffer, J. R., Muench, A. A., Rieke, G. H., Lada, E. A., Bouvier, J., & Lada, C. J. 2003, *ApJ*, 593, 1093
- McLean, I. S., et al. 2000, *ApJ*, 533, L45
- McGovern, M. R., Kirkpatrick, J. D., McLean, I. S., Burgasser, A. J., Prato, L., & Lowrance, P. J. 2004, *ApJ*, 600, 1020
- Meyer, M. R. 1996, Ph.D. Thesis
- Meyer, M. R., Calvet, N., & Hillenbrand, L. A. 1997, *AJ*, 114, 288
- Muench, A. A., Alves, J., Lada, C. J., & Lada, E. A. 2001, *ApJ*, 558, L51
- Muench, A. A., Lada, E. A., Lada, C. J., & Alves, J. 2002, *ApJ*, 573, 366
- Muench, A. A., et al. 2003, *AJ*, 125, 2029
- Nakajima, T., Oppenheimer, B. R., Kulkarni, S. R., Golimowski, D. A., Matthews, K., and Durrance, S. T. 1995, *Nature*, 378, 463.
- Natta, A., Testi, L., Comerón, F., Oliva, E., D'Antona, F., Baffa, C., Comoretto, G., & Gennari, S. 2002, *A&A*, 393, 597
- Oppenheimer, B. R., Kulkarni, S. R., Matthews, K., Nakajima, T. 1995, *Science*, 270, 1478.
- Ortiz, R., & Lepine, J. R. D. 1993, *A&A*, 279, 90
- Padoan, P., & Nordlund, Å. 2002, *ApJ*, 576, 870
- Padoan, P., & Nordlund, Å. 2004, *ApJ*, 617, 559
- Pickett, B. K., Durisen, R. H., Cassen, P., & Mejia, A. C. 2000, *ApJ*, 540, L95
- Rebolo, R., Zapatero-Osorio, M. R., & Martín, E. L. 1995, *Nature*, 377, 129
- Reid, I. N., et al. 1999, *ApJ*, 521, 613
- Reid, I. N., Burgasser, A. J., Cruz, K. L., Kirkpatrick, J. D., & Gizis, J. E. 2001, *AJ*, 121, 1710
- Reipurth, B., & Clarke, C. 2001, *AJ*, 122, 432
- Robberto, M., Song, J., Mora Carrillo, G., Beckwith, S. V. W., Makidon, R. B., & Panagia, N. 2004, *ApJ*, 606, 952
- Slesnick, C. L., Hillenbrand, L. A., & Carpenter, J. M. 2004, *ApJ*, 610, 1045
- White, R. J., Ghez, A. M., Reid, I. N., & Schultz, G. 1999, *ApJ*, 520, 811
- Whitworth, A. P., & Zinnecker, H. 2004, *A&A*, 427, 299
- Wilking, B. A., Greene, T. P., & Meyer, M. R. 1999, *AJ*, 117, 469
- Wilking, B. A., Meyer, M. R., Greene, T. P., Mikhail, A., & Carlson, G. 2004, *AJ*, 127, 1131

TABLE 1
FLAMINGOS SPECTROSCOPIC OBSERVATIONS

Mask ID	Telescope	Observation Date	t_{exp}	N_{exp}
n2024bd1	4m	2003 Jan 19	600s	8
oc24mf11	4m	2003 Dec 06	300s	8
oc24mf21	4m	2003 Dec 10	300s	13
n2024b2	4m	2004 Dec 01	300s	10
n2024b3	4m	2004 Dec 01	300s	10
n2024f31	2.1m	2003 Nov 29	300s	14

TABLE 2
YOUNG SPECTRAL STANDARDS

ID	R.A.	Dec.	Optical Spectral Type
I348-052	03:44:43.53	+32:07:43.0	M1
I348-122	03:44:33.22	+32:15:29.1	M2.25
I348-207	03:44:30.30	+32:07:42.6	M3.5
I348-095	03:44:21.91	+32:12:11.6	M4
I348-266	03:44:18.26	+32:07:32.5	M4.75
I348-230	03:44:35.52	+32:08:04.5	M5.25
I348-298	03:44:38.88	+32:06:36.4	M6
I348-329	03:44:15.58	+32:09:21.9	M7.5
I348-405	03:44:21.15	+32:06:16.6	M8
I348-603	03:44:33.42	+32:10:31.4	M8.5
KPNO-Tau4	04:27:28.01	+26:12:05.3	M9.5

NOTE. — Spectral types for the IC 348 objects are the spectral types adopted by Luhman et al. (2003b) and found in table 2 of that work. The spectral type for KPNO-Tau4 was determined by Briceño et al. (2002).

TABLE 3
MEASURED DATA AND DERIVED QUANTITIES FOR CLASSIFIED SOURCES IN NGC 2024

Source	FLAMINGOS ID	J	H	K	M Subclass ^a	A_V	r_K	$\log T_{eff}$	$\log(L/L_\odot)$	Mass (M_\odot)
01	FLMN_J0541378-0153112	12.06	11.07	10.30	<M
02	FLMN_J0541344-0154409	12.25	11.07	10.37	1.75	4.73	0.19	3.558	0.125	0.72
03	FLMN_J0541366-0154082	13.71	11.91	11.07	4.00	10.82	-0.11	3.514	-0.012	0.29
04	FLMN_J0541402-0150522	14.11	12.20	11.29	1.75	11.36	-0.03	3.558	-0.004	0.72
05	FLMN_J0541373-0151403	15.54	12.81	11.29	1.75	18.82	0.09	3.558	0.264	0.72
06	FLMN_J0541333-0151270	13.64	12.00	11.37	1.75	8.91	-0.13	3.558	-0.124	0.70
07	FLMN_J0541293-0151304	13.22	11.96	11.43	2.50	5.59	-0.05	3.544	-0.292	0.55
08	FLMN_J0541456-0151229	14.64	12.69	11.65	3.50	12.18	-0.01	3.524	-0.195	0.29
09	FLMN_J0541436-0151353	15.30	12.80	11.66	4.00	17.18	-0.20	3.514	-0.019	0.29
10	FLMN_J0541390-0151453	15.10	12.87	11.69	4.75	14.70	-0.06	3.499	-0.146	0.17
11	FLMN_J0541443-0155247	15.29	13.01	11.69	2.75	14.93	0.12	3.539	-0.067	0.54
12	FLMN_J0541417-0151457	14.06	12.49	11.75	4.50	8.64	-0.09	3.504	-0.380	0.20
13	FLMN_J0541496-0153270	14.77	12.83	11.79	2.75	11.84	0.04	3.539	-0.218	0.54
14	FLMN_J0541578-0151278	13.57	12.24	11.81	1.50	6.09	-0.14	3.562	-0.393	0.68
15	FLMN_J0541569-0150331	14.18	12.55	11.84	2.75	9.32	-0.12	3.539	-0.350	0.44
16	FLMN_J0541566-0155526	13.58	12.38	11.92	5.25	5.48	-0.17	3.488	-0.587	0.13
17	FLMN_J0541259-0150243	14.36 ^b	12.94	12.20	5.25	7.48	-0.05	3.488	-0.627	0.13
18	FLMN_J0541313-0154052	14.13	12.78	12.23	2.75	6.73	-0.13	3.539	-0.623	0.28
19	FLMN_J0541350-0153286	14.42	13.08	12.41	4.75	6.61	-0.04	3.499	-0.725	0.17
20	FLMN_J0541316-0152318	14.42	13.13	12.49	5.50	6.36	-0.08	3.483	-0.791	0.12
21	FLMN_J0541438-0151399	17.57	14.30	12.52	4.50	24.09	-0.06	3.504	-0.131	0.20
22	FLMN_J0541489-0152297	16.19	13.82	12.65	<M
23	FLMN_J0541350-0155300	16.81	14.37	12.67	5.50	16.82	0.30	3.483	-0.487	0.12
24	FLMN_J0541501-0155320	18.04	14.65	12.73	4.75	25.25	-0.01	3.499	-0.182	0.17
25	FLMN_J0541506-0158041	14.33	13.36	12.77	7.75	3.49	-0.05	3.431	-1.084	0.03
26	FLMN_J0541379-0153187	16.18	14.20	12.94	4.75	12.43	0.16	3.499	-0.727	0.17
27	FLMN_J0541460-0150071	14.91	13.64	12.98	5.00	6.05	-0.03	3.494	-0.982	0.17
28	FLMN_J0541364-0154412	15.60	13.93	12.98	7.25	10.25	-0.10	3.443	-0.907	0.04
29	FLMN_J0541456-0157332	14.25	13.45	12.99	8.00	1.15	-0.05	3.425	-1.264	0.03
30	FLMN_J0541314-0154347	16.15	14.24	13.00	3.25	11.86	0.24	3.529	-0.723	0.35
31	FLMN_J0541469-0151099	15.55	13.84	13.01	4.25	9.95	-0.08	3.509	-0.828	0.25
32	FLMN_J0541514-0152470	15.59	13.96	13.03	5.75	9.59	-0.02	3.478	-0.900	0.10
33	FLMN_J0541588-0150311	15.12	13.84	13.10	5.25	6.20	0.03	3.488	-1.033	0.15
34	FLMN_J0541413-0150300	16.33	14.28	13.12	5.00	13.14	0.01	3.494	-0.783	0.15
35	FLMN_J0541281-0152138	15.10	13.85	13.19	5.25	5.93	-0.03	3.488	-1.078	0.15
36	FLMN_J0541359-0153371	15.57	14.07	13.22	7.25	8.70	-0.10	3.443	-1.059	0.04
37	FLMN_J0541480-0152198	16.03	14.22	13.25	5.25	11.02	-0.05	3.488	-0.919	0.13
38	FLMN_J0541439-0153513	16.83	14.84	13.28	3.00	12.36	0.62	3.534	-0.810	0.37
39	FLMN_J0541461-0151442	18.86	15.30	13.37	7.00	27.05	-0.18	3.449	-0.450	0.04
40	FLMN_J0541345-0152135	15.55	14.20	13.37	8.00	6.16	-0.01	3.425	-1.236	0.03
41	FLMN_J0542029-0152038	16.13	14.45	13.42	5.50	9.91	0.06	3.483	-1.036	0.12
42	FLMN_J0541390-0155008	17.66	14.98	13.43	6.00	19.27	-0.04	3.472	-0.720	0.09
43	FLMN_J0541528-0150162	15.71	14.33	13.50	7.50	8.00	-0.09	3.437	-1.205	0.03
44	FLMN_J0541387-0150507	16.11	14.54	13.56	6.75	8.98	0.02	3.455	-1.168	0.05
45	FLMN_J0541508-0152236	15.77	14.38	13.57	5.50	7.27	0.02	3.483	-1.191	0.13
46	FLMN_J0541523-0157123	15.75	14.35	13.57	5.75	7.50	-0.03	3.478	-1.191	0.11
47	FLMN_J0541475-0150052	15.96 ^b	14.47	13.62	4.75	7.98	0.04	3.499	-1.160	0.19
48	FLMN_J0541377-0155097	16.99	14.93	13.65	7.75	13.40	-0.01	3.431	-1.079	0.03
49	FLMN_J0541514-0152408	17.02	14.97	13.67	6.50	13.36	0.07	3.461	-1.045	0.06
50	FLMN_J0541372-0151580	17.28	14.96	13.69	4.75	15.52	-0.03	3.499	-0.916	0.20
51	FLMN_J0541534-0156482	15.60	14.35	13.70	4.00	5.82	0.01	3.514	-1.244	0.23
52	FLMN_J0541537-0157503	16.30	14.73	13.70	6.50	9.00	0.08	3.461	-1.215	0.06
53	FLMN_J0541506-0153064	16.54	14.86	13.71	8.25	9.12	0.10	3.419	-1.274	0.03
54	FLMN_J0541340-0149391	18.05	15.36	13.75	4.25	18.86	0.11	3.509	-0.803	0.24
55	FLMN_J0541497-0156198	...	15.88	13.76	7.00	29.11	-0.14	3.449	-0.531	0.04
56	FLMN_J0541374-0152311	16.40	14.77	13.76	6.75	9.52	0.02	3.455	-1.228	0.05
57	FLMN_J0541328-0151271	15.91	14.64	13.82	8.50	5.36	0.01	3.412	-1.461	0.02
58	FLMN_J0541366-0154151	17.24	15.32	14.00	7.50	12.91	0.07	3.437	-1.228	0.03
59	FLMN_J0541501-0151180	16.13	14.86	14.02	7.50	7.00	-0.02	3.437	-1.449	0.03
60 ^d	FLMN_J0541390-0151316	17.86	15.64	14.19	4.00	14.64	0.24	3.514	-1.123	0.24
61	FLMN_J0541357-0153483	16.40	15.03	14.21	2.75	6.66	0.16	3.539	-1.373	0.37
62	FLMN_J0541287-0155264	16.44	15.02	14.24	7.25	7.98	-0.12	3.443	-1.493	0.04
63	FLMN_J0541380-0151536	17.56	15.63	14.37	4.75	11.98	0.19	3.499	-1.316	0.16
64 ^d	FLMN_J0541483-0151304	17.44	15.60	14.42	5.00	11.23	0.15	3.494	-1.371	0.14
65	FLMN_J0542020-0153542	16.68	15.31	14.50	6.25	7.27	-0.01	3.466	-1.588	0.07
66	FLMN_J0541345-0154500	17.10	15.54	14.61	7.75	8.85	-0.06	3.431	-1.626	0.03
67	FLMN_J0541547-0151461	17.74	16.11	15.05	8.00	8.70	0.05	3.425	-1.816	0.03
68	FLMN_J0541250-0152267	13.74 ^b	12.25	11.59	5.00 ^c	8.05	-0.14	3.494	-0.399	0.15
69	FLMN_J0541338-0153087	13.83	12.48	11.75	6.75 ^c	6.98	-0.09	3.455	-0.516	0.05
70	FLMN_J0541269-0154093	13.88	12.72	12.04	2.50 ^c	4.68	0.16	3.544	-0.568	0.47
71	FLMN_J0541368-0154479	15.54	13.43	12.07	7.25 ^c	14.25	0.03	3.443	-0.399	0.04

^aSpectral types are listed as M subclasses, thus a table entry of 0.0=M0.0, 7.50=M7.50, etc.

^bSources 17, 47, and 68 have J magnitudes derived from FLAMINGOS imaging on the 2.1m telescope.

^cSources 68-71 have spectral types derived from 2.1m spectroscopy.

^dPossible background giant.

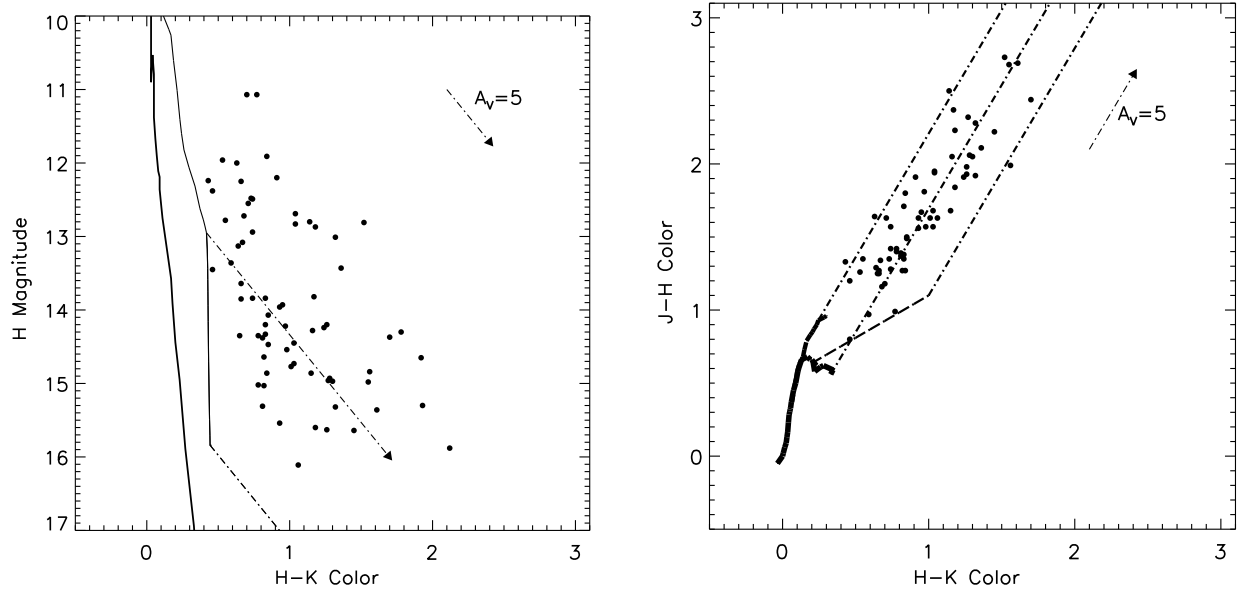


FIG. 1.— Color-magnitude (left) and color-color (right) diagrams for all classified objects in NGC 2024. In the CMD, the leftmost solid line is the main sequence from Bessell & Brett (1988) and to the right is the 0.3 Myr isochrone of D’Antona & Mazzitelli (1997). The dot-dashed lines are reddening vectors using the extinction law of Cohen et al. (1981) placed at 0.08 and $0.02 M_{\odot}$. In the color-color diagram, the solid lines are the giant colors of Bessell & Brett (1988) coupled with a combination of Bessell & Brett (1988) dwarf colors for spectral types down to K7 and Leggett (1992), Leggett et al. (1996), and Dahn et al. (2002) for spectral types from M0 to M6. The dot-dashed lines are the reddening vectors of Cohen et al. (1981) and the dashed line is the classical T Tauri locus of Meyer et al. (1997).

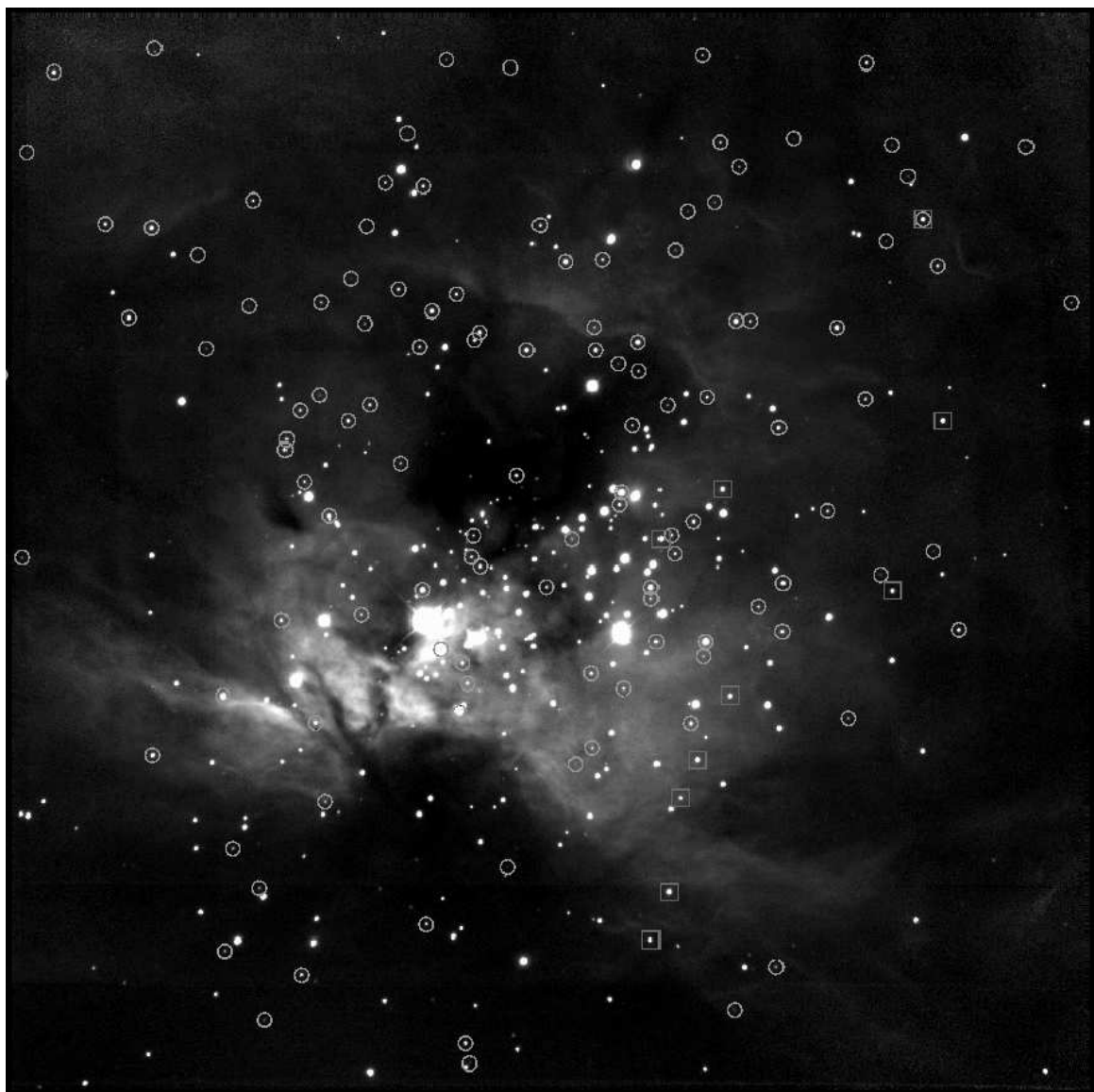


FIG. 2.— K-band image of NGC 2024 taken with FLAMINGOS on the KPNO 4m telescope. North is up, East is to the left, and the field is approximately 10' on a side. Circled objects are all 4m spectroscopic targets and rectangles enclose the 2.1m targets.

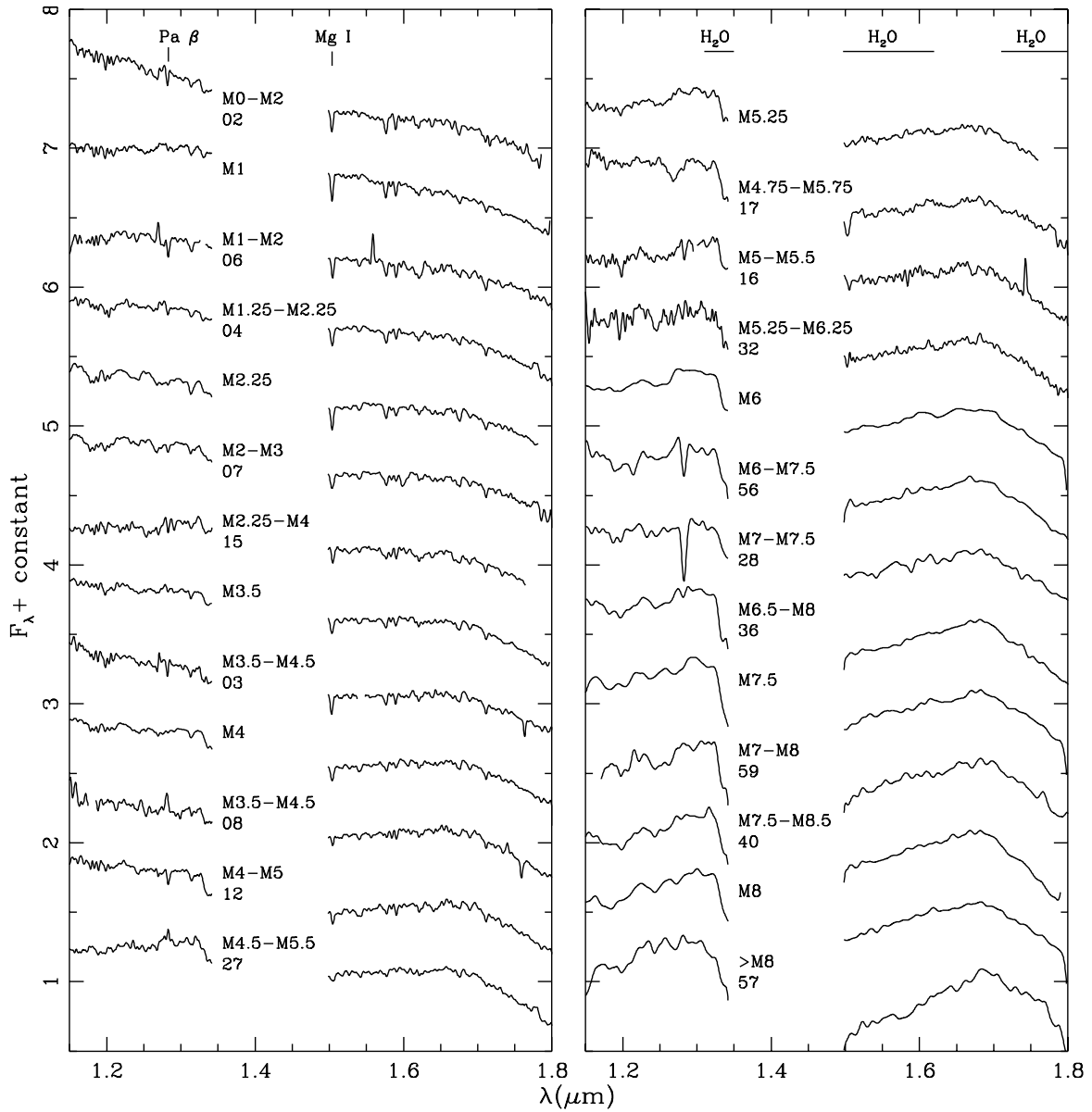


FIG. 3.— M spectral sequence for young objects in NGC 2024 (labeled with both spectral type and ID) shown with the IC 348 optically classified young standards (labeled with spectral type only). Prominent spectral features are identified at the top. Objects having spectral types $<M6$ have been smoothed to $R \sim 500$ and objects $\geq M6$ have been smoothed to $R \sim 200$ to aid in the classification process. The central regions of the spectra are blocked out for display purposes because in most cases the signal to noise in these regions is very low due to the overwhelming telluric absorption. No usable information is lost from these regions.

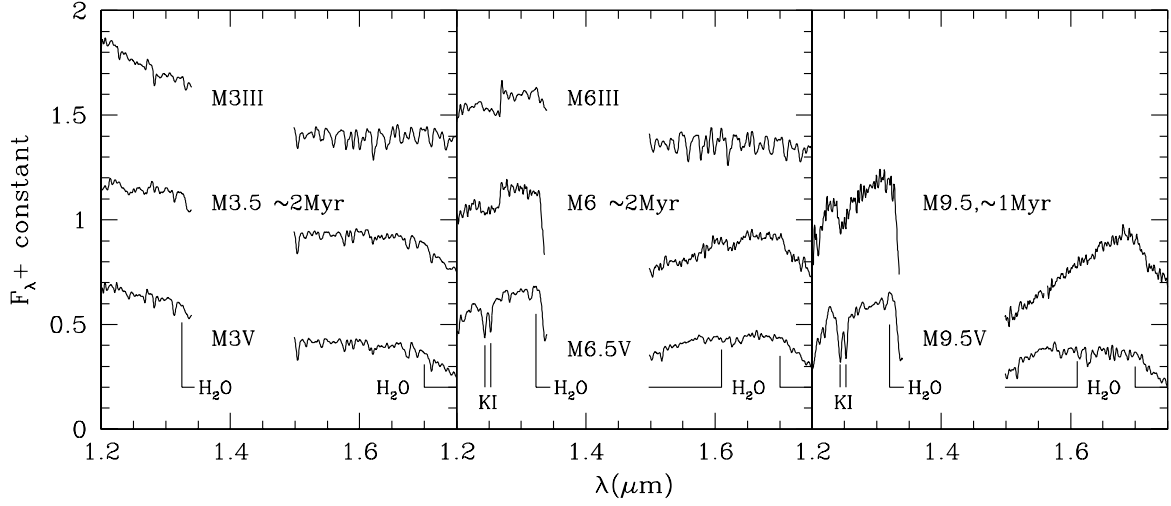


FIG. 4.— FLAMINGOS spectra of the young objects I348-207 (M3.5), I348-298 (M6), and KPNO-Tau4 (M9.5), shown with spectra of the field dwarfs Gl 388 (M3V), GJ 1111 (M6.5V), LHS 2065 (M9.5V) and the M Giants HD 39045 (M3III) and HD 196610 (M6III). The most prominent gravity sensitive features at $R \sim 500$ are labeled. The spectra of both giants appear to have a much higher H-band line frequency than the young objects or field dwarfs. In addition, water absorption causes the younger objects to have a much more triangular H-band shape which can be used to distinguish field stars from young cluster members.

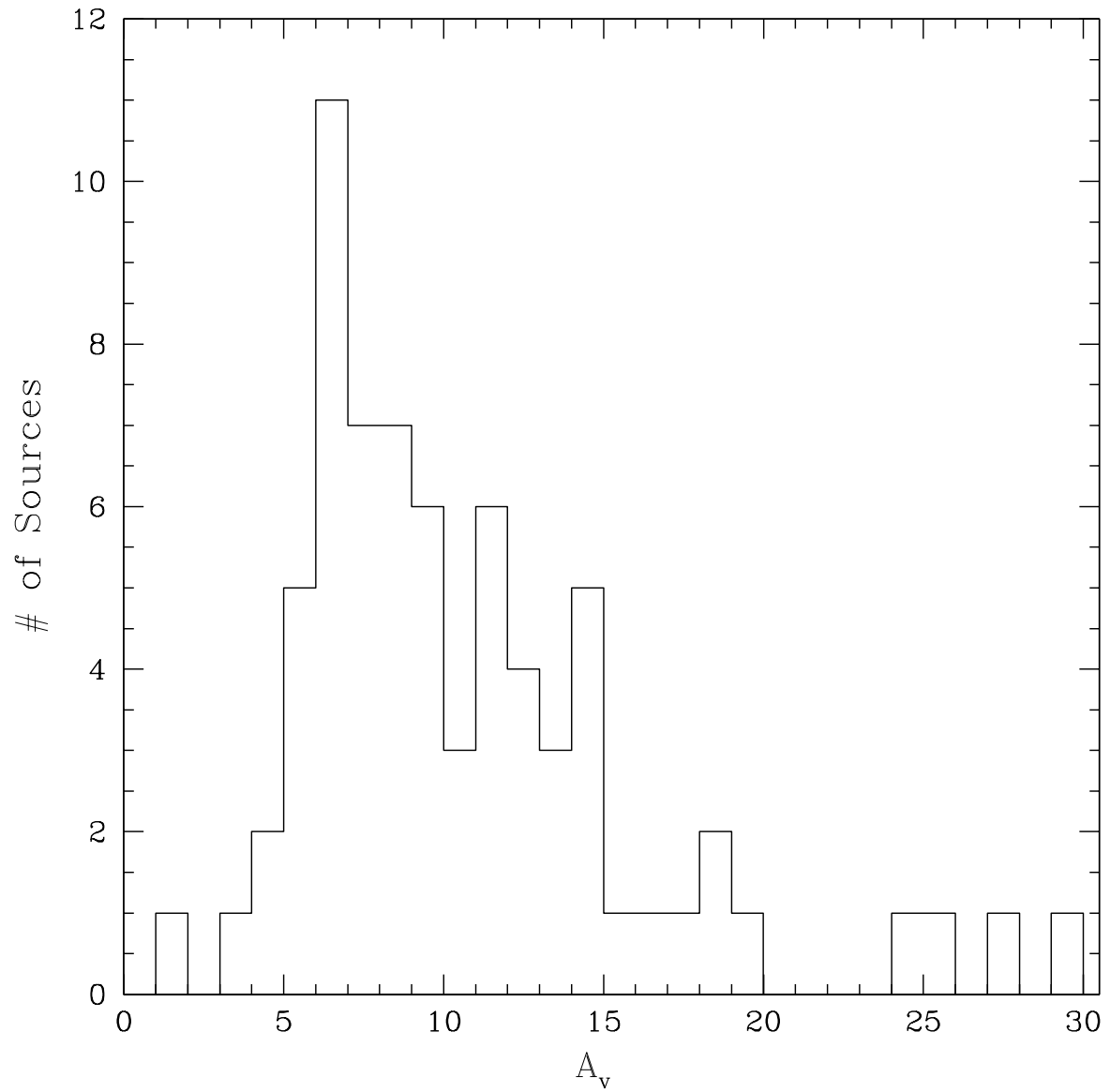


FIG. 5.— Distribution of visual extinctions for the spectroscopic sample. A_V values were derived by comparing observed $J-H$ colors with the intrinsic $J-H$ colors of Leggett (1992); Leggett et al. (1996); Dahn et al. (2002).

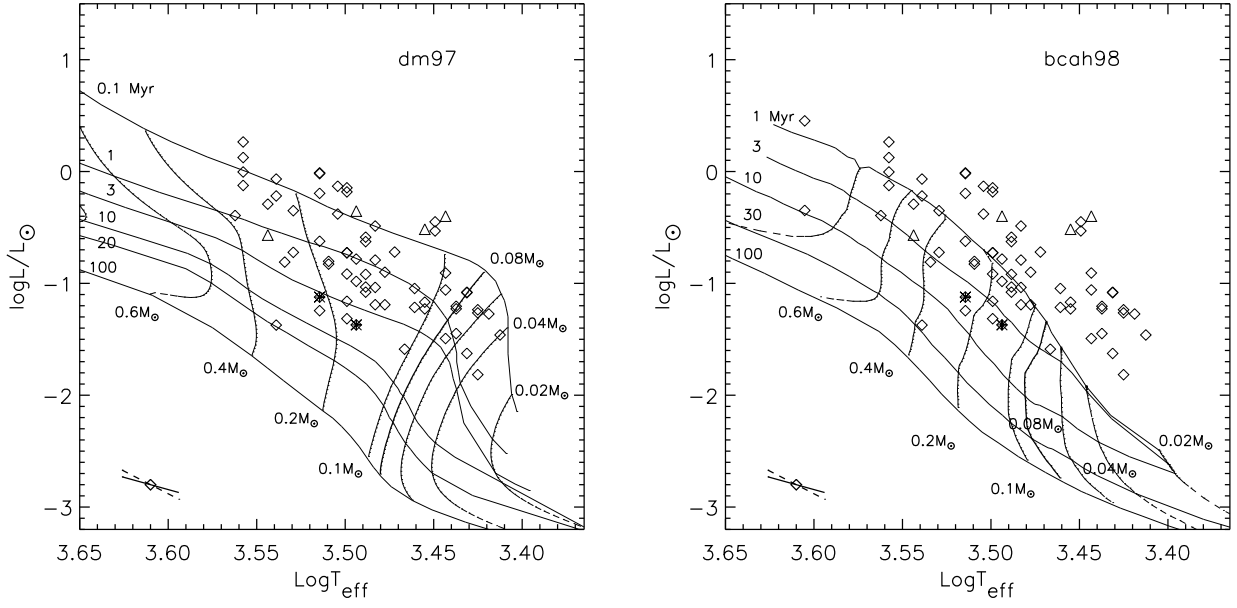


FIG. 6.— H-R Diagrams for NGC 2024 shown with the pre-main sequence models of D’Antona & Mazzitelli (1997) (left) and Baraffe et al. (1998) (right). The diamonds represent points with 4m spectra and the triangles are sources classified with 2.1m spectra. Asterixes are potential background giants. Representative error bars for an M5 object are shown. The solid line accounts for errors in derived spectral type, distance modulus, and photometry and the dashed line incorporates an additional error of ± 3 magnitudes of visual extinction (see §4.1).

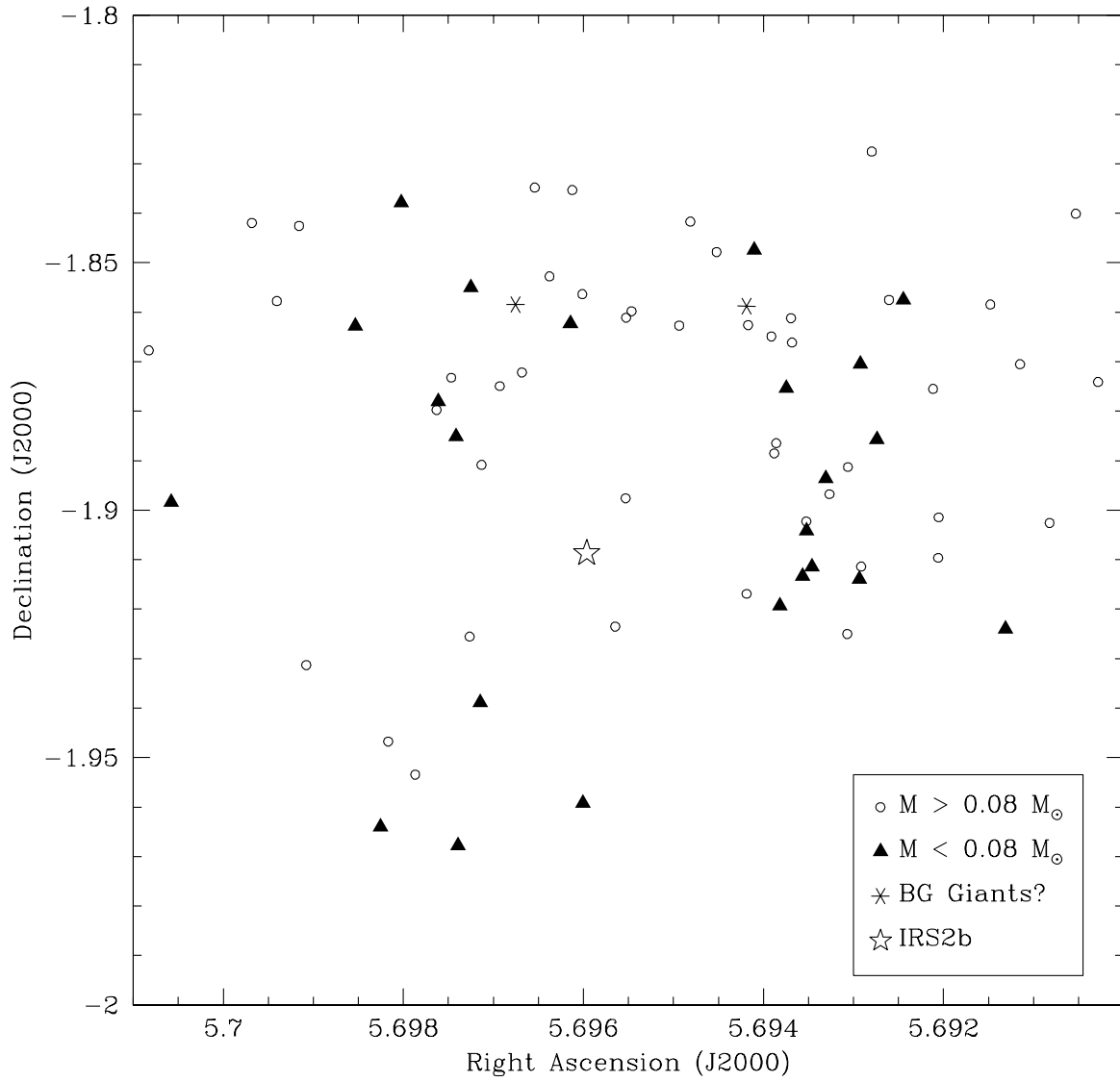


FIG. 7.— Spatial distribution of both stellar and substellar objects in NGC 224. The open circles represent objects with masses $M > 0.08 M_{\odot}$, filled triangles are objects with $M < 0.08 M_{\odot}$, asterixes are possible background giants, and the star represents IRS2b.

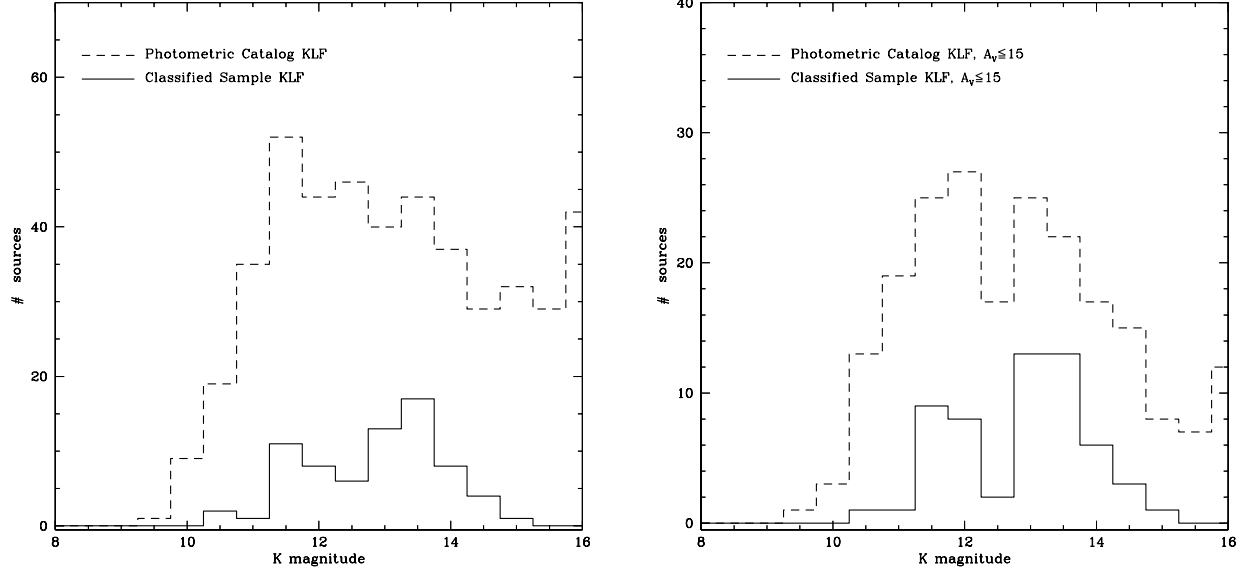


FIG. 8.— *Left:* K -band luminosity function for all classified objects in the spectroscopic sample (solid line) shown with the KLF for the photometric catalog (dashed line). *Right:* KLFs for both samples with an imposed extinction limit of $A_V \leq 15$. It can be seen from the figure that in the magnitude range $11.25 < K < 14.75$ the extinction-limited spectroscopic sample is representative of the extinction-limited main cluster population.

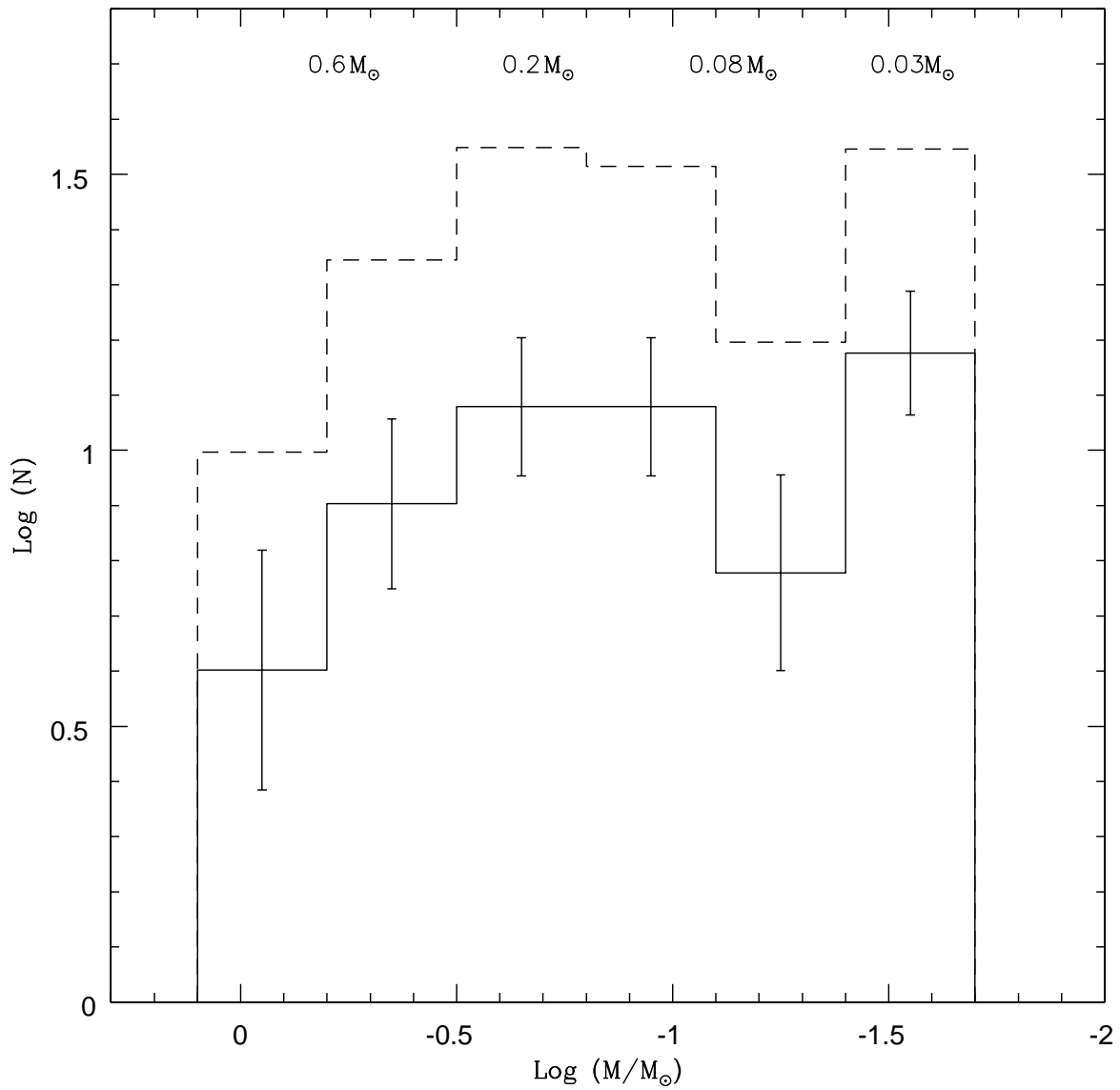


FIG. 9.— Mass function for all classified objects in NGC 2024 whose spectra indicate that they are cluster members with spectral types $\geq M0$. The solid line is the uncorrected raw mass function shown with Poisson error bars and the dashed line has been corrected for magnitude incompleteness in the range from $11.25 < K < 14.75$.